

Towards a morphology diagram for terrestrial carbonates: evaluating the impact of carbonate supersaturation and alginic acid in calcite precipitate morphology

Ramon Mercedes-Martín^{1*}, Mike Rogerson², Tim J. Prior³, Alexander T. Brasier⁴, John J.G. Reijmer⁵, Ian Billing^{6,†}, Anna Matthews⁷, Tracy Love⁷, Scott Lepley⁷, and Martyn Pedley⁸

1. SZALAI Grup S.L., P.O Box 1005, Caimari, 07314, Spain (*info@ramonmercedes.com).

2. Department of Geography and Environmental Science, Ellison Building, Northumbria University, Newcastle, UK, NE1 8ST

3. Department of Chemistry & Biochemistry, University of Hull, Cottingham Road, Hull, UK, HU6 7RX4.

4. School of Geosciences, Meston Building, University of Aberdeen, Old Aberdeen, Scotland, UK, AB24 3UE.

5. College of Petroleum Engineering & Geosciences, King Fahd University of Petroleum & Minerals, Dhahran, Saudi-Arabia, 31261.

6. University of Derby, Kedleston Road, Derby, UK, DE22 1GB.

7. BP Exploration - Integrated Subsurface Description & Modelling, Bldg H, Desk W172 25

Chertsey Road, Sunbury on Thames, UK, TW16 7LN 26.

8. Department of Geography, Geology and Environment, University of Hull, Cottingham Road, Hull, UK. HU6 7RX.

† Deceased

This manuscript is a preprint published on March 28th, 2021 in the preprint server EarthArXiv. It has also been submitted for publication in *Geochimica et Cosmochimica Acta*.

Although the contents of this preprint are true and complete according to the authors; future versions may have slightly different wording or figures.

Please contact the lead author Ramon Mercedes-Martín (info@ramonmercedes.com) if you have any questions or comments about this preprinted manuscript.

ABSTRACT

Ancient and recent terrestrial carbonate-precipitating systems are characterised by a heterogeneous array of deposits volumetrically dominated by calcite. In these environments, calcite precipitates display an extraordinary morphological diversity, from single crystal rhombohedral prisms, to blocky crystalline encrustations, or spherulitic to dendritic aggregates. Despite many decades of thorough descriptive and interpretative work on these fabrics, relating calcite micro-morphology with sedimentary hydrogeochemical conditions remains a challenge. Environmental interpretations have been hampered by the fact that calcite morphogenesis results from the complex interaction between different physico-chemical parameters which often act simultaneously (e.g., carbonate mineral supersaturation, Mg/Ca ratio of the parental fluid, organic and inorganic additives). To try to experimentally address the sedimentological causes of calcite morphogenesis, an experimental approach yielding a first attempt at a calcite growth-form phase diagram is presented here. The initial aim was to account for the carbonate products experimentally nucleated in alkaline, saline lake settings. These are the result of at least two competing calcite precipitation ‘driving forces’ that affect morphogenesis: the calcite supersaturation level of the parental fluid, and the concentration of microbial-derived organic molecules (alginic acid). A key finding of this study is that common naturally-occurring calcite products such as calcite floating rafts, rhombohedral prismatic forms, di-pyramid calcite crystals, spherulitic calcite grains, or vertically stacked spheroidal calcite aggregates, can be related to specific hydrogeochemical contexts, and their physical transitions pinpointed in a phase diagram. By exploring binary or ternary responses to forcing in morphological phase-space, links between calcite growth forms and (palaeo)environmental conditions can be determined. This provides a truly

process-oriented means of navigating questions around carbonate precipitate morphogenesis for the future.

Keywords: calcite, morphology, alkaline, terrestrial, saturation index, alginic acid

Running title: Calcite morphology phase diagram for terrestrial carbonates

1. INTRODUCTION

Terrestrial carbonate systems in lakes, springs, rivers, caves, and soils may form spectacular and complex deposits that are volumetrically dominated by calcite (Pentecost, 2005). The morphology of the calcite formed is extremely diverse, ranging from blocky crystalline encrustations (Frisia et al., 2000), through regular but non-unit cell (Pedley et al., 2009) geometric forms such as triads to exotic radial, dumb-bell, feather, dendritic and spherulitic morphologies (e.g., Jones, 1994; Jones and Renaut, 1995; Rainey and Jones, 2009; Pedley and Rogerson, 2010; Renaut et al., 2013; Jones and Peng, 2014; Pedley, 2014; Erthal et al., 2017; Jones, 2017). Careful and thoroughgoing observation across several generations of geoscientists has provided us with a large knowledge base of where forms occur, and their spatial association (see Jones, 2017). However, relating these forms to environmental parameters remains challenging due to the dynamic nature of the environments in which they occur. Consequently, our ability to relate the genesis of different growth forms, to understand why one form gives way to another, or to predict what growth form will occur in any given type of system (and vice versa) is seriously hampered. This has consequences for our understanding of how the terrestrial carbonate archive records variations in past

environments. This is a major problem, considering terrestrial carbonates host important hydrocarbon (Wright 2012) and precious metal (Daliran 2008) reserves as well as globally significant archaeological (Smith et al. 2007, Meyer et al. 2017) and palaeoclimatic records (Andrews 2006, Andrews and Brasier 2005; Boch et al., 2015; 2018; McCormack et al., 2019), form key sinks for pollutants in systems affected by hyperalkaline contamination (Gomes et al., 2017), or precipitate as unwanted scale deposits compromising the exploitation of geothermal waters (Boch et al., 2017; Regenspurg et al., 2015)

1.1. Unlocking the Archive

To understand the environmental significance of natural calcite growth morphologies, we seek a mechanistic understanding of why crystals assemble with a particular structure: in other words, we aim to find a way to link growth form(s) and condition(s) to processes in the parental solution. Here, we build on parallel advances in the materials science community. The latter use calcite as a ‘guinea pig’ crystal form to understand the fundamental controls on solid material construction and biominerals (e.g., Meldrum and Cölfen 2008). The simplest form of morphological control arises from the ‘driving force’ of the precipitation reaction (Oaki and Imai 2003). At low ‘driving force’ (e.g. moderate supersaturation), the crystal forms at equilibrium with its morphology controlled by the shape of the unit cell. As driving force increases, formation of new mineral mass increasingly occurs through disordered polycrystal nucleation, and the rate of mineral growth becomes limited by diffusion rather than reaction kinetics (Oaki and Imai 2003). A high driving force leads first to dendritic polycrystal forms with highly disequilibrium morphology, progressing towards dense, disordered branching growth, and ultimately, when a very extreme driving force applies, leads to spherular radial forms. Addition of a wide range of dissolved materials within the

parental solution can also have a major effect on the crystal growth form (Meldrum and Cölfen 2008), but interactions between different additives make the prediction of the crystal form challenging (Meldrum, pers. comm., 2016). Inorganic and organic additives, both soluble and insoluble, can induce, impede or alter precipitation (Morse et al., 2007; Seto, 2012; Reddy and Hoch, 2012; Montanari et al., 2016). For example, at high magnesium to calcium ratios magnesium can impede calcite formation (Sun et al. 2015). However, at lower ratios the same additive can control the orientation of self-assembled monolayers without significant impedance of the crystallisation reaction (Han et al. 2005). Organic additives can enhance or impede calcite production but can also cause preference of a different polymorph of calcium carbonate, or even promote formation of stable amorphous calcium carbonate (Aizenberg et al. 1996; Addadi et al., 2003; Rivadeneyra et al., 2010).

For continental carbonate rocks, contexts will rarely be so simple that a morphological change can be ascribed to a single additive; the effects will always be summative for these complex mixtures. However, sedimentologists can harness the progress that has been previously made in materials science laboratories to develop a conceptual framework in which individual morphologies can be organised, related and understood (Cölfen and Qi, 2001; 2016; Rao et al, 2016).

1.2. Phase diagrams: a new, old approach

Binary phase diagrams are used to illustrate how two environmental conditions (e.g., grain size and flow velocity) combine to control a range of sedimentary growth morphologies (bedforms) and have been used within clastic sedimentology ever since proposed by Harms et al. (1982). Different phase diagrams have been compiled for many different clastic environments, from rivers (Lapotre et al., 2017; Baas, et al., 2016; Southard and Boguchwal,

1990) to the deep ocean (Stow et al., 2013). Recently, apparently disruptive parameters such as biological and mineralogical cohesion have been investigated, constrained, and provided a third axis within the phase diagram system, rather than a truly confounding barrier to their use (Schindler et al., 2015). Today, the idea of a bedform phase diagram remains fundamental within clastic sedimentology, virtually unchanged from the original concept.

Here, a new growth-form phase diagram method is proposed for naturally occurring calcite precipitates. Inspired by recent debate about the origin of spherulitic fibro-radial calcite allochems formed in alkaline, lacustrine systems (Wright, 2012; Saller et al., 2016; Sabato-Ceraldi and Green, 2016; Mercedes-Martín et al., 2016, 2017, 2019; 2021; Rogerson et al., 2017; Bastianini et al., 2019), a salty, highly alkaline fluid composition was used for the case study. Following evidence from the materials science literature (Meldrum and Cölfen, 2008; Song and Cölfen, 2011) that the strongest controls on morphology arise from the rate of crystal growth (here we induce changes by manipulating calcite supersaturation) and the presence of organic additives (here we use the relatively well known additive alginic acid), we present a *binary* study in which the combined and independent controls from these two different environmental parameters are plotted in a way that is analogous to bedform diagrams used by clastic sedimentologists. The system response we show herein will also be sensitive to the molar ratio of carbonate and calcium, ionic strength (i.e. salinity), the hydraulic condition of the solution, the ratio of magnesium and calcium, the composition of the organic additive, the concentration of sulphate, phosphate, or the composition of the pre-nucleation surfaces on which we observe calcite formation. We therefore do not offer this case study as a ‘final answer’, but as a methodological framework to experimentally capture the environmental influences in calcite morphogenesis in a way that can be easily accessible for sedimentologists and paleoclimatologists. In this study, we experimentally investigate the

effects that carbonate saturation state and alginic acid content have on: i) calcite petrography and aggregation patterns, ii) loci of calcite precipitation, and iii) calcium and magnesium removal rates from solutions. Although we do not include isotopic composition, trace element geochemistry and non-calcite mineral formation here, such additional factors could be analysed in future studies.

2. METHODS AND MATERIALS

2.1. Parental batch preparation and experimental set-up

A parental solution was synthetically prepared to be similar to waters in Mono Lake, California (Connell and Dreiss 1995), though being initially supersaturated with respect to CaCO_3 phases (calcite) and having initial alkalinities between 16,60 and 129 meq/L (Table 1). Experiment preparation was carried out in a stainless steel horizontal laminar flow cabinet equipped with a UV-C lamp to prevent microbial contamination. Synthetic lake water (parental solution) was prepared by adding powdered/ pearl reagent-grade anhydrous $\text{Ca}(\text{OH})_2$, together with $\text{Mg}(\text{OH})_2$, Na_2SiO_3 and H_3BO_3 to deionised water (18 $\text{M}\Omega\text{-cm}$) which was systematically bubbled with CO_2 using a soda stream mechanism. To achieve sterility, powdered chemicals, frosted glass slides, tweezers, and glassware were heat-sterilised by autoclave at 160°C for two hours. CO_2 -rich deionised water was autoclaved in an ASTELL Sterilizer at a maximum of 121°C and 1700 milibars for two hours. Items that could not be heat-sterilised, such as tubing and plastic pipette tips, were treated with 16% hydrogen peroxide solution overnight.

2.2. Experimental preparation

The pH of the parental solution was then adjusted to 7, 8, 9, 10, 11 and 12 by adding enough NaOH pearls, and the concentration of alginic acid varied between 0 mg/L, 0.01 mg/L, 0.1 mg/L, 0.5 mg/L, and 1 mg/L through serial dilutions under the same standards of sterility. Once the targeted pH was reached using a glass-bodied Jenway 3510 pH meter electrode, aliquots of the parental batch solution were passed through sterile 0.22 µm diameter MF-Millipore filters, and redistributed and assayed in four 100ml conical glass flasks, each containing sterilised 1 cm² frosted glass slides. By so doing we ensured that the solution entering the conical flasks did not contain either biological remains or crystals that did not form during the duration of the experiment. After this stage, the selected alginic acid concentration was added to every 100 ml conical glass flask. Total alkalinities of the initial experimental solutions (TA_i) were systematically measured using a Mettler-Toledo T50 digital titrator and a DGi117-water pH electrode with a Rondolino autosampler (Table 2). After alkalinity measurements, the flasks were sealed by air-permeable but microbe-impermeable foam stoppers and agitated by an orbital flask shaker at 120 rpm to ensure mixing of their contents. Experiments ran for 3 days (pH 11 and 12) or 10 days (pH 7, 8, 9 and 10) at 25°C in a controlled environment cabinet under dark conditions.

2.3. Sampling and microscopic observations

After experiment termination, pH was measured again with a glass-bodied Jenway 3510 pH meter electrode, the solution was sampled, and the frosted slides were autoclaved at 105°C for one hour (Table 2). Visual inspection was performed to determine whether crystal precipitation took place on the surface of the flasks (neck or bottom) or at the air-water interface. Formation and abundance of polymer hydrogels was also monitored visually.

Friable precipitates were collected by using a Büchner glass funnel with attached sterilised cellulose nitrate filters (0.2 μm), which were routinely autoclaved at 40°C for 1 hour. Frosted slides were removed from the flasks by using sterilised tweezers. Dried slides and friable material were mounted directly on an aluminium stub, carbon coated and observed with a Zeiss EVO60 Scanning Electron Microscope (SEM). SEM imaging and measurements were performed at beam currents of 40 μA and 20 kV EHT accelerating voltage. Elemental X-ray analyses were also conducted with an Inca System350 Energy Dispersive X-ray Spectrometer (EDX). X-ray powder diffraction data was collected from the glass slides and friable material was mounted in stainless steel sample holders. Measurements were performed between 20 and 50 degrees (2Θ range) on solids. A PANalytical Empyrean diffractometer operating in Bragg-Brentano geometry with copper $K\alpha_1$ ($\lambda = 1.540546 \text{ \AA}$) and a PIXEL detector was used for data collection.

Concentrations of Ca, Mg, and Na (Table 2) were measured at experiment termination using a Perkin Elmer Optima 5300DV inductively coupled optical emission spectrometer (ICP-OES). The selection of the analytical lines used was based on the Perkin Elmer recommendations for the Optima 5300DV spectrometer, 393.366 nm for calcium and 280.271 nm for magnesium and 589.562 nm for sodium. Calibration standards were prepared using 1000 ppm standard stock solutions (99.9% pure or greater, PrimAg, Xtra, Romil, Cambridge) of calcium and magnesium. Samples were diluted with 5% ultrapure HNO_3 to bring the expected concentrations within or near to the linear calibration of the standards. Saturation indexes (acronym: SI) of the relevant mineral phases, solution ionic strength, and Ca^{2+} and CO_3^{2-} activities (expressed as $\{\text{Ca}^{2+}\}$ and $\{\text{CO}_3^{2-}\}$), and initial Total Alkalinity (TA_i) were calculated using the geochemical software PHREEQC (Parkhurst and Appelo,

2013) (Table 2). Furthermore, calcium and magnesium average removal rates were also obtained (see Table 2).

2.4. Terminology

Abiotic precipitation. We refer here to calcium carbonate precipitated due to inorganic, physico-chemical processes with *no influence* of organic molecules, microbial exopolymeric substances or microbial metabolisms (e.g., Chafetz and Guidry, 1999). Experiments falling within this category can be considered as control experiments.

Organomineralisation. We refer here to calcium carbonate precipitated due to inorganic physico-chemically forced processes but under the *influence* of organic molecules from living organisms (*sensu* Trichet and Défarge, 1995 or Défarge, 2006). We note that our solutions were designed to be sterile, and that the alginic acid used in the experiments is known to be synthesised from living microbial cells. Alginates are linear copolymer polysaccharides composed of β -1,4 linked D-mannuronic (M) and L-guluronic (G) acids present in certain algae (Kloareg and Quatrano, 1988). The M and G units are arranged in a block-wise manner with homopolymeric M and G blocks interspaced with alternating MG blocks (Haug et al., 1974).

Single crystals are here referred to crystalline solids in which the crystal lattice of the entire sample is continuous and unbroken to the edge of the sample, with no grain boundaries (Meldrum and Cölfen, 2008; Zhou and O'Brien, 2008). In most instances, single crystals are characterised by a regular internal structure with smooth and planar external faces (Meldrum and Cölfen, 2008); however, single crystals with curved surfaces are also formed in nature (e.g. biominerals) where crystals grow in the presence of organic substances (Young et al, 1999; Meldrum and Cölfen, 2008).

Polycrystals refer to polycrystalline solids formed of aggregates of numerous grains or elongated crystallites representing the basic crystallographic units (Cölfen and Antonietti, 2008; Imai, 2016). Polycrystals can grow through the random aggregation of small ‘crystal building blocks’ (Imai, 2016).

3. EXPERIMENTAL RESULTS

3.1. Petrographic domains and terminology

The scheme in Figure 1 shows the photomicrographs of the most characteristic crystal morphotypes reported in association to specific SI and alginic acid contents. Figures 2 and 3, summarises the morphotypes and the distribution patterns of benthic and floating calcite crystals. In latter diagrams, three types of occurrences were characterised: i) Lower Layer Crystals (LLC), ii) Upper Layer Crystals (ULC), and iii) Floating Crystals (FC). LLC are calcite crystals that nucleated on top of the frosted slide. ULC refers to those crystals that nucleated on top of previously formed LLC crystals, and FC are crystals that nucleated at the air-water interface. LLC and ULC are considered as benthic crystals hereafter. Figures 4A-B show the seven different calcite petrographic domains established from Figures 2 and 3 on the basis of the dominant microscopic assemblages. Domains are labelled as: ‘*Surface crusts*’, ‘*Elongated prisms*’, ‘*Di-pyramid*’, ‘*Rhombic*’, ‘*Dumb-bell*’, ‘*Spherical*’, and ‘*Stacked spherical*’. An eighth domain could also be recognised (labelled as ‘*No calcite*’) and is characterised by the absence of calcite precipitation.

The terminology used for each petrographical domain (e.g., ‘*Di-pyramid*’, ‘*Rhombic*’) attempts to label the volumetrically most abundant calcite growth form recognised despite a diversity of petrographies can coexist *within* a single domain (see Figure 3). The limits

between crystal domains tend to be demarcated by distinct changes in crystal morphology, either for benthic and/ or floating calcite crystals.

Figure 4C illustrate the correspondence between petrographic domains and the precipitation styles: abiotic precipitation and organomineralisation (see Section 3.2). Figures 5 to 9, S1 and S2 display the SEM photomicrographs showing the diversity of calcite crystals and EDS spot analyses for every petrographic domain. XRD data is supplied in Figure S3.

3.1.1. Domain 1: No calcite precipitation

The lowest part of the diagram in Figures 1 and 4 represent a domain where calcite crystal formation was not seen by SEM inspection. Such regions represent the lowest SI values (0.87 and 1.81) in the experiments. Exceptions are two discrete regions (0.01 and 0.5 mg/L of alginic acid) where calcite crystals did occur (see domain 2, and Figures 1, 3 and 4).

3.1.2. Domain 2: Surface crusts

The lowest part of the diagram (Figures 1, 3 and 4) is characterised by the occurrence of two isolated regions where complex mineral mixtures including calcium carbonate, sodium chloride and amorphous silicate-like phases precipitated (Figures 4A- B; 5A to D). EDS and XRD revealed a Na, Cl, Mg, and Si-rich composition (see Figure S3). This domain is essentially characterised by the following precipitates (Figure 5 C to F): i) acicular calcite fan bodies (400 μm in diameter) intermingled with each other and covering flat surfaces (Figure 5C, D), ii) structureless banded calcite overgrowths (up to 10 μm -thick) with individual or aggregated circular crystals (40 μm -diameter, Figure 5 E-F), and iii) tiny cubic euhedral to thin and smooth coatings of sodium chloride crystals (up to 30 μm in diameter, Figure 5F) . Such crystal assemblages are exclusively formed under the lowest SI conditions (0.87 and

1.81) coupled with particular concentrations of alginic acid (0.5 and 0.01 mg/L, respectively) (Figure 4).

3.1.3. Domain 3: Elongated prisms

This domain shows two benthic petrographic morphotypes (Figures 1, 3 and 4): i) subhedral to anhedral, double-terminated trigonal to tetragonal elongated prismatic forms (up to 15 μm -length, Figure 6A); and ii) subhedral to anhedral, trigonal flat prismatic and faceted calcite crystals (10 μm -length) (Figure 6A). Inter-grown twinning between prismatic crystals is observed (Figure 6A). Floating raft clusters made up of imbricated elongated prismatic crystals (up to 20 μm in diameter) and trigonal flat prismatic/faceted crystals (up to 30 μm in diameter) are recognised growing at the air-water interface (Figure S1 A-B). This domain is the lowest SI where air-water interface precipitates were recorded. All these petrographic assemblages occur under a SI of 2.46 and a solution devoid of alginic acid.

3.1.4. Domain 4: Di-pyramids

This petrographic region is dominated by abundant benthic di-pyramid (Figures 6B-E; 7A) and tetragonal trapezohedron calcite crystals (Figure 6C, E), which are well developed under a SI of 2.46 and invariably in the presence of alginic acid (between 0.01 and 1 mg/L, Figures 1, 2, 3 and 5). Additional morphological assemblages include: i) ‘rose-like’ calcite spheroidal particles (Figure 6E; Figure S1D), ii) subhedral calcite di-pyramids with protruded and rounded corners (Figures 6D, 7A-B, Figure S1E), and ii) rare tetrahedron calcite particles (Figure 6B; Figure S1C-D).

Di-pyramid crystals are subhedral to euhedral and up to 40 μm in diameter, growing as individual bodies (Figure 6B-C) or clusters of imbricated twins forming relatively dense

layers as benthic precipitates (Figure 6B; 7B). Granular textures embedded within dried alginic acid gels were identified when the solution was enriched in organics (>0.01 mg/L, Figure 6E). In the high organic-content part of this domain, di-pyramid crystals with protruded and rounded corners (up to $20\ \mu\text{m}$ in diameter) are stacked vertically generating patchy clusters with positive reliefs (up to $400\ \mu\text{m}$ in diameter, Figure S1E). Moreover, subhedral to euhedral tetragonal calcite trapezohedrons (up to $50\ \mu\text{m}$ in diameter) with curved faces are common as individual crystals which eventually form massive crusts (Figure 6C, E).

Individual ‘rose-like’ spheroidal particles with subhedral rhombic imbricated crystals (up to $20\ \mu\text{m}$ in diameter) can coalesce to form clusters (up to $100\ \mu\text{m}$ in length) or dense layers’ hundreds of microns in length (Figures 6E; S1F). Floating raft components were recognised as tightly fitted crusts of spherulitic calcite bodies (up to $30\ \mu\text{m}$ in diameter) coated by dense and homogeneous dodecahedron calcite crystals (Figure S2A).

3.1.5. Domain 5: Rhombic

This domain is formed by highly packed, anhedral to subhedral tiny rhombic calcite crystals (up to $3\ \mu\text{m}$ in diameter) forming dense crusts (Figures 1, 3, 4). Globular clusters (gc) of these rhombic crystals (up to $40\ \mu\text{m}$ in diameter) are periodically recognised (Figure 7C). This petrographic assemblage developed under moderate-high SI (2.81) and absence of alginic acid.

3.1.6. Domain 6: Dumb-bell

This petrographic region (see Figures 1, 3, 4) is mainly characterised by calcite forming tetrahedron crystals (Figure 7D), and dumbbell fibro-radial calcite spherules (Figure 7D-E).

Extensive crusts of tightly packed subhedral tetrahedron calcite crystals (up to 3 μm in diameter) are covered by random clusters of dumbbell fibro-radial calcite spherules (up to 20 μm in diameter) which tend to grow vertically (Figure 7D-E).

Floating raft occurrences growing at the air-water interface display trigonal flat prismatic and faceted calcite crystals forming laterally linked aggregates growing into crusts (Figure 7F).

The downward vertical stacking of trigonal flat crystals produces pyramid calcite bodies overlain by up to 3 μm in diameter subhedral tetragonal and subhedral to euhedral prismatic calcite crystals. This petrographic assemblage is exclusively formed under moderate to high SI conditions (2.81 to 2.85) and marginal concentrations of alginic acid (0.01 mg/L).

3.1.7. Domain 7: Spherical

This is an extensive petrographic region, occurring only under the highest SI conditions (Figures 1, 3, 4) and is made up of spheroidal fibro-radial calcite particles (up to 45 μm in diameter) and dumbbell fibro-radial spherules laterally packed as lower layer precipitates (Figure 8). The lateral accretion produces extensive and tightly packed crusts with faded hemispherical outlines. Spherulites are normally coated by dense and homogeneous layers of either i) euhedral/subhedral rhombic (Figures 8A, C, D, F) or reinforced rhombic imbricated calcite crystals (Figure 8E), or ii) subhedral tetrahedron calcite crystals (Figure 8B).

Individual tiny (up to 3 μm in length), elongated tetrahedron crystals are recognised as the seeds of up to 10 μm in diameter spherular aggregates (Figure S2B). In experiments with higher organic contents (>0.01 mg/L), dried alginic acid was identified by SEM covering spherulitic particles, which is consistent with the visual observation of tiny calcite precipitates suspended within polymeric hydrogels in the flasks during the experiments (compare Figure S4B with C).

Floating raft components were identified growing at the air-water interface developing fibro-radial spheroidal calcite forms. Up to 500 μm in length, laterally densely fitted fibro-radial spheroidal calcite particles grow towards the downward side of flat annular crusts. Such particles are coated by rhombic to reinforced rhombic euhedral calcite crystals (Figure S2C-D). Crusts tend to accrete inwards until total occlusion. Enhanced vertical epitaxial growth is recurrent in solutions with increased contents of organics (0.1 to 1 mg/L).

3.1.8. Domain 8: Stacked spherical

This petrographic domain has been demarcated within Domain 7 (Spherical crystals) and is characterised by the enhanced aggregation of vertically growing spheroidal calcite grains (either fibro-radial or protruded di-pyramids; Figure 9A and Figures 9C and S2E, respectively) producing isolated and closely packed globular and ‘shrubby’ clusters (up to 300 μm in diameter) (Figures 1, 3, 4 and 9). Elongated globular bunches expanding laterally are also observed (up to 600 μm in length, Figure S2F). Remains of dried alginic acid are observed surrounding isolated protruded di-pyramid crystals, and their globular clusters form only in solutions tested at higher concentrations of alginic acid (0.5-1 mg/L, Figure 9A). In this subdomain, floating raft components up to 500 μm in length were also identified forming fibro-radial spheroidal calcite particles covered in subhedral rhombic calcite crystals (Figure 9E). Enhanced vertical epitaxial growth is very common where organics abounded (e.g., 0.1 and 0.5 mg/L).

3.2. Abiotic precipitation vs organomineralisation: summary of crystal domains

Domains 3 and 5 are characterised by the occurrence of growthforms that can be unambiguously attributed to abiotic precipitation in the present study (Figure 4C). However, growthforms characteristic from domain 7 can occur both in the field of abiotic precipitation and organomineralisation. Moreover, either di-pyramid crystals (domain 4) and stacked spherical crystals (domain 8) occur under the influence of contrasting alginic acid concentrations indicating that alginic acid influenced their formation (organomineralisation). Similarly, calcites in domains 2 and 6 seems to be exclusively formed when alginic acid is present in specific concentrations being also considered as organomineralisation products.

3.3. Mineralogy, loci of precipitation and hydrogel formation

Figure 10 summarises the mineralogies, location of calcite precipitates and the occurrence of hydrogels documented during the course of the experiments. The lower part of the diagram represents a region dominated by amorphous Mg-silicate-like phases ('No calcite precipitation'), and low-Mg calcite minerals ('Surface crusts'). Conditions prevailing in Domains 3 to 6 (i.e. 'Elongated prisms', 'Di-pyramid', 'Rhombic', 'Dumbdell') promoted the massive formation of calcium carbonate displaying Low-Mg to Mg calcite mineralogies; Mg-calcite minerals are suppressed by moderate (0.01-0.5 mg/L) alginic acid concentrations. Furthermore, the high SI region of the diagram ('Spherical' and 'Stacked spherical') is dominated by low-Mg calcite mineralogies. Amorphous Mg-silicate phases are only recognised in regions with either low SI values and diverse alginic acid contents, or high SI conditions regardless of organic concentration, indicating a complex relationship between these parts of the system.

Visual inspection demonstrates that all petrographic domains apart from 'Surface Crusts' recorded calcite precipitation consistently either at the bottom (as benthic precipitates) and in

the neck of the flasks (air-water-glassware contact). The domains of ‘No calcite’ and ‘Surface Crusts’ registered amorphous Mg-silicate-like phase (data not shown), and calcite minerals respectively, and both exclusively as benthic products (Table 3).

The lower SI limit for the formation of floating calcite crystals is observed in the domain of ‘Elongated prisms’ (zero organic influence combined with low supersaturation), while the upper limit for raft nucleation occurs in the upper part of the ‘Spherical’ Domain (diverse alginic contents combined with very high alkalinity). Consequently, raft nucleation is impeded by organic additives at low saturation but sustained by them at high saturation. In the ‘Spherical’ Domain, the heterogeneous presence of alginic acid hydrogels can be directly correlated with the occurrence of floating calcite rafts. In the ‘Rhombic’, ‘Dumbbell’ and ‘Spherical’ Domains, the association between presence of organics/ hydrogels and calcite raft formation is not straightforward (Table 3).

3.4. Ca and Mg removal

Table 4 shows the average percentage of Ca and Mg removal for any given SI between 0.87 and 2.86 and for each experimental treatment with alginic acid. More than 90% of calcium is removed in experiments performed above the limit of $SI = 2.46$, encompassing most of the petrographic domains (Table 4). Experiments with $SI: 2.85$ and alginic acid: 0.01 mg/L record minor Ca removal rates (66.33%) corresponding with the ‘Dumbbells’ and ‘Elongated prisms’ domains, though a clear relationship between growth form and Ca removal is not consistently observed. Furthermore, in experiments with high concentrations of organic acids (lower part of Table 4) Ca removal rates are only slightly impacted, indicating that the mass of calcium bound to organic acid molecules was likely dependant on the saturation state of the solution itself.

The average magnesium removal shows percentages above 75% in all of the petrographic domains and SI regions (Table 4) These results suggest that alginic acids did not impact overall Mg removal, indicating a low inventory for organic-bound Mg compared to solution and mineralogical Mg.

4. DISCUSSION

4.1. Effects of solution chemistry and alginic acid concentration in calcite precipitation rates and mineralogies

In order to assess the calcite crystal morphology from a thermodynamic point of view, their shape is presented (Figures 1, 3 and 4) in combination with the calcite saturation index (SI). This more accurately encompass the relation between the calcium and carbonate ion concentrations of the precipitating solution.

The lowest rates of calcium and magnesium precipitation (between 4-11 mg/day) were recognised under the lowest SI (0.87 and 1.81, respectively; Domain 1) (Table 2) when carbonate to calcium activity ratios were extremely low. Under these conditions, magnesium-rich amorphous silicate-like solids were preferentially formed over calcite. Ca removal rates notably increased under the increased presence of polymers (see Tables 2 and 4). This phenomenon, however, did not seem to enhance calcite formation nor influence the precipitate morphology.

The addition of specific concentrations of alginic acids contributed to low-Mg calcite precipitation in the 'Surface Crusts' domain indicating that particular organic acid levels reduce the interfacial energies for carbonate precipitation and have an apparent impact on the partition of $(Mg/Ca)_{\text{calcite}}$ (Saunders et al., 2014) (Figures 4 and 10). Moreover, the production

of abundant Mg-rich phases in the ‘Surface Crusts’ domain can explain why low-Mg calcite mineralogies are predominant over Mg calcite.

The Mg-calcite deposition reported in the ‘Prism’, ‘Di-pyramid’, ‘Rhombic’, and ‘Dumbbell’ domains, with Ca removal values of ~31 to 34 mg/day (Table 2) is interpreted to result from the tenfold to thirtyfold increase in carbonate to calcium activity ratio compared to the ratio registered in Domain 1 and 2 permitting diffusion-limited, heterogeneous precipitation of the mineral.

In the higher calcite supersaturation region (‘Spherical’ and ‘Stacked spherical’ domains), Ca or Mg removal values did not significantly change with alginic acid presence. In addition, the highest Ca and Mg removal values are interpreted as a consequence of pH speciation effects produced by increased CO_3^{2-} concentrations (Ca = ~102 to 111 mg/ day; Table 2). In such supersaturated conditions polymer presence did not meaningfully affect the removal of calcium indicating that precipitation was likely ‘abiotic’ and triggered by purely physico-chemical mechanisms (i.e., SI), rather than driven by polymer intervention or ‘organomineralisation’ processes (e.g., Cölfen and Song, 2011; Rao et al., 2016; Jones, 2017).

The precipitation of low-Mg calcite over Mg-calcite in the top of the diagram (‘Spherical’ and ‘Stacked spherical’ domains, Table 3) can be explained by the observation that the filtered solution entering the flasks was already depleted in Mg further promoting higher calcium removal values (Table 2). This is supported by the presence of Mg-rich carbonate powder in the residue as analysed from the parental solution prepared at high saturation index (Figure S4A).

All the experiments were performed under the same controlled laboratory conditions, so evaporation rates were similar and do not create “unfair test” conditions. Although this may

have caused some random variation, it was not sufficient to undermine the systematic and reproducible changes we describe in this work.

4.2. Effects of solution chemistry and alginic acids in calcite morphology and loci of precipitation

As predicted by many experimental studies, carbonate supersaturation and organic additive concentration are paramount parameters controlling the morphology of carbonate crystals, from rhombic to polygonal to dendritic or spherulitic (Cölfen and Qi, 2001; Braissant et al., 2003; Sunagawa, 2005; Mao and Guang, 2007; Cölfen and Song, 2011; Kim et al., 2017; Kosanović et al., 2017; Zhang et al., 2017). However, studies dealing with the experimental quantification of the physical impact that supersaturation levels and organic additives have in calcite precipitate morphology in these material chemistry experiments are difficult to relate to *naturally* occurring settings (e.g., Frisia et al., 2000; Taylor et al., 2004). Diverse carbonate fabrics can be observed, for example, in a single speleothem sample from Italian Alpine caves, including columnar, fibrous, and microcrystalline carbonate textures (Grotta del Calgeron, Frisia et al., 2000). Despite detailed environmental parameters are postulated to control speleothem fabrics (water discharge, dripwater SI, or presence of impurities), a quantitative verification of the links between the invoked processes and the observed calcite fabrics remains elusive.

Our results show that, in solutions similar to those found in nature, precipitation of ‘single-crystal’ prismatic morphologies occurs at low supersaturation conditions, and ‘polycrystal’ spherulitic morphologies tend to form when solutions are highly supersaturated (*sensu* Oaki and Imai, 2003; Jones, 2017). In experiments with no alginic acid, calcite precipitation

occurred both as benthic crystals and at the air-water interface as floating rafts regardless of the saturation index, implying two different mechanisms of crystallisation. Calcite produced at the air-water interface can be assumed to be related to gas exchange forcing, but benthic precipitates reflect bulk solution properties and precipitation can only be preconditioned by gas exchange, not forced by it. Both benthic and floating crystals show analogous morphologies as we move towards the region of higher calcite saturation (e.g., ‘Spheroidal’ Domain, Figures 1, 3 and 4), indicating that the two mechanisms become difficult to distinguish under these conditions, particularly in the absence of organics. Increasing alginic acid concentrations exacerbated the stacking patterns of the crystals grown as floating and benthic precipitates (see ‘Di-pyramid’ and ‘Dumbbell’ domains, Table 3). This reflects that under higher SI the presence of alginic acid did not alter the basic crystallographic unit (‘Spheroids’). However, alginic acid modified the aggregation patterns of these units due to the binding of ions in the hydrogel matrix and the selective blocking of kink sites on calcite crystal surfaces (Meldrum and Cölfen 2008).

Indeed, the chelating nature of alginic acid towards aqueous cations such as Ca^{2+} allows specific interactions with calcite crystallography (Perry IV et al., 2006; Rao et al., 2016; Kosanović et al., 2017). Most environmental alginic acid tend to be deprotonated at the carboxylate functionalities leading to torsional intermolecular arrangements compatible with calcite crystallisation following preferred spatial orientations (Perry IV et al., 2006; Li et al., 2007; Ma and Feng, 2011). These biopolymers form stable hydrogels following distinct steps of Ca^{2+} binding, such as ion complexation, dimerization, and lateral association of biomolecules with helical conformations (Fang et al., 2007; Rao et al., 2016). During the first step the formation of monocomplexes between Ca^{2+} and the G units of alginic acid takes place by collapse/ shrink of alginate chains. During the second step, the formation of 1D

'egg-box' dimers tends to occur by the pairing of monocomplexes. The last step is associated to the formation of 'egg-box' multimers composed of helical chains that aggregate laterally and vertically forming larger intermolecular growths (Fang et al., 2007; Rao et al., 2016). This pattern in structural alginic acid assembly can explain the space-limited calcite nucleation forming stacking of calcite spherical crystals within the biopolymer hydrogel (Domain 8, Figure 9).

Moreover, in the region characterised by moderate SI conditions (lower part 'Di-pyramid' domain, Figures 4 and 10), an increase in alginic acid abundance inhibited calcite raft formation implying suppression of gas exchanged-forced precipitation in favour of precipitation within diffuse alginic acid matrices. This outcome confirms previous observations inferring that the physical location of crystallisation is *commonly* modified by the presence of extracellular polymers, causing calcite to preferentially nucleate in the bottom of the water masses, rather than in the air-water interface (Bonny and Jones, 2003; Jones and Peng, 2014; Mercedes-Martín et al., 2016). This pattern also supports previous findings that the presence of benthic biofilms tends to induce less precipitation at the air-water interface, and more at channel bottoms in flowing water settings (Rogerson et al., 2008; Pedley et al., 2009).

Increasing dissolved organic acid content enhanced the sphericity of the calcite crystals, turning trigonal-tetragonal elongated prism morphologies (Domain 3) into di-pyramid forms and tetragonal trapezohedrons (Domain 4) (Figures 1, 3 and 4) as also demonstrated in biomimetic experiments (Rao et al., 2016). This behaviour relates to the specific binding of alginic acid disaccharide networks to surface-step edges enhancing a confined calcite nucleation process favouring the formation of curved and poorly faceted crystal

morphologies (Orme et al., 2001; Perry et al., 2006; Fang et al., 2007; Rao et al., 2016). Effectively, the transition between ‘Elongated prisms’ to ‘Di-pyramids’, or ‘Dumbbell’ to ‘Di-pyramids’ encompass a macroscopic reduction of crystal faceting that was promoted by the increase in biopolymer concentrations. Interestingly, in all high supersaturation experiments (SI = 2.86) the organic-influenced effects on crystal faceting are much less obvious. This likely indicates that the ‘driving’ force of the layering of spheroidal morphologies is largely related to bulk solution properties (SI, ‘abiotic precipitation’) rather than polymer interference (‘organomineralisation’). Furthermore, the formation of dodecahedron, rhombic imbricated, and tetrahedron calcite crystals covering the spherulitic particles that characterise the domain of ‘Spherical’ crystals (Figure 8) reflect declining saturation as the calcium and carbonate reservoir in the flask is exhausted during the evolution of the experiments, effectively moving late precipitates in these settings ‘one row down’.

The presence of high organic contents, including the formation of millimetre-thick alginic acid hydrogel lumps (Fig. S4B, C), most likely results in the enhanced aggregation of vertically growing ‘spheroidal’ fibro-radial calcite grains on the glass slides (‘Di-pyramid’ and ‘Stacked spherical’ crystals). SEM observations of dried alginic hydrogels enveloping individual spheroidal grains and their aggregates (Figure S4B) show that calcite crystals subaqueously epitaxially nucleated on top of each other rather than being gravitationally stacked during slide autoclaving. Indeed, the mineral assemblies recognised in dried gels can be explained by progressive complexation of Ca^{2+} ions into the molecular structure of the alginic acid leading to confined calcite mineral nucleation and subsequent crystallisation forming larger clusters.

In addition, the presence of tiny calcite precipitates suspended in polymeric hydrogels further suggests that vertical ‘shrubby’ calcite (‘Stacked spherical’ crystals) was organically mediated within diffuse hydrogels (Figure S4B). Interestingly, ‘Stacked spherical’ crystals (high SI) display an enhanced vertical aggregation compared to ‘Di-pyramid’ crystals (lower SI), even under high organic additive concentration. This suggests that either a) alginic acid exhibits a pH-dependent behaviour over its stereochemical architecture, calcite nucleation times and pre-nucleation slopes (Rao et al., 2016), and that the geometric arrangement of the calcium binding sites is likely affected by rising alkaline conditions (Perry et al., 2006; Rao et al., 2016); or b) that, unlike sphericity itself, high supersaturation does not eliminate the control of biopolymers on mineral stacking patterns. This likely reflects a macroscale control on crystal assembly within hydrogel bodies, rather than a kink site impact of biopolymers on crystal assembly itself.

4.3. Calcite growth-form phase diagrams: applications for sedimentology

Phase diagrams are extremely powerful interpretive tools to convert qualitative observations about a sediment into quantitative constraints on the environment where it was deposited, and in relating different forms in terms of trends in environmental conditions of different sites. The diagram presented here for non-marine calcite sediments (Figure 4) shows the competing influence of the chemical ‘driving force’ of the precipitating solution (calcite saturation index) and the degree of influence with crystal growth from acidic organic additives (alginic acid). Terrestrial carbonate precipitating systems generally show a strong variability reflecting diurnal, seasonal, climatic or tectonic influences (Arenas et al., 2014; Cappezuoli et al., 2014). Multiple factors can act simultaneously and independently to modify both calcite growth rates and crystal morphology (e.g., Mg/Ca ratio, flow hydraulics, evaporation degree, metabolic

processes; SO_4^{2-} , PO_4^{2-} or NaCl concentrations; different organic/ inorganic molecules or time). These controlling parameters all provide potential future variables to be evaluated by further experiments. However, from a methodological perspective, the approach presented in this paper has produced for the first time a quantifiable, repeatable link between biogeochemical conditions present within an environment, and carbonate petrographic signatures. This link opens the possibility to quantitatively reconstruct palaeo-environments in the same way as analogous phase diagrams allow ancient hydraulic conditions to be reconstructed from siliciclastic bedforms (e.g., van den Berg and van Gelder, 1993).

The calcite growth-form diagrams can aid in understanding non-marine carbonate precipitates, which will be illustrated in three examples: i) floating rafts, ii) di-pyramidal forms, and iii) shrubby calcite growth (Figure 4).

4.3.1 Calcite floating rafts

Our observations suggest that calcite floating rafts can form by gas exchange at the air-water interface regardless of the presence of organic acids (e.g. ‘Elongated prisms’, ‘Dumbbell’ and ‘Spherical’ crystals, Figure 4). However, the range of specific calcite morphologies observed growing at the downward part of the rafts varies from trigonal-tetragonal elongated prisms (Figure 7F) to densely fitted spheroidal calcite overgrowths (Figures 9D, E) to trigonal flat prismatic shapes (Figure S1A-B), or spheroidal with rhombic coatings (Figures S2A, C, D). The spheroidal shapes develop similar to benthic crystals of the same morphology and show the same phase behaviour in the saturation-organic inhibition matrix. Hence, the formation of the rafts like those shown in Figure 4 (Domain 3, ‘Elongated prisms’) occurs under moderate supersaturated conditions without alginic acid intervention. The presence of dissolved organics

will generate rafts with strikingly different calcite crystal morphologies as predicted by our diagram (see Taylor et al., 2004).

4.3.2. *Di-pyramidal forms*

Calcite with tetragonal to di-pyramidal morphologies has been documented from natural freshwater environments as discrete deposits around cellular material in green algae and microbial mats (Schneider, 1977; Chafetz and Buczynski, 1992). Laboratory and field studies demonstrate that di-pyramidal calcite morphotypes preferentially form abiotically in the presence of a viscous gelled medium, mostly composed of polysaccharides or hydrolysed proteins (e.g., Chafetz and Buczynski, 1992; Chekroun et al., 2004 and references therein). These authors highlighted the importance of organic gelled matrices in the formation of these precipitates which have not been reported in absence of organic additives. Our experiments reinforce the statement that similar ‘Di-pyramidal’ crystals are *exclusively* nucleated under the influence of different concentrations of alginic acid following a comparable growth mechanism as the one described for the gel-grown pseudo-octahedral assemblies by Grassmann et al., 2003. However, we can also report that they form only under moderate alkalinity (SI), and so will not be found in sites with remarkably high saturation even in the presence of organic acids (Figures 4 and 6B to F).

4.3.3. *Shrubby calcite growth*

The growth of millimetre- to centimetre-scale ‘shrubby’ calcite has been recently documented in some volcanic lacustrine settings of the ‘Pre-salt’ Aptian lakes (Terra et al., 2010; Herlinger et al., 2017). Such components display vertical epitaxial growth of spherulitic to bundles of fibrous calcite crystals producing branching to arbustiform macrocrystals (Saller et al., 2016;

Herlinger et al., 2017; Farias et al., 2019). Analogous ‘shrubby’ carbonate fabrics have been described from continental geothermal settings in Tivoli by Erthal et al. (2017). These authors associated its origin to changes in the hydrodynamic conditions in waterlogged areas. However, our study shows that the formation of vertically stacking micrometre-scale spherulitic calcite aggregates (‘Stacked spherical’) can arise from agitated flowing waters as flasks were shaken during experiments. The experiments also demonstrate that stacked spherulitic crystal habits require *both* the intervention of abundant biopolymer hydrogels *and* higher supersaturation conditions to develop (Figure 9), being considered as organomineralisation products (Figure 4C). This is consistent with recent findings for shrubby calcites grown in steel-slag Anthropocene settings (Bastianini et al., 2019), and lacustrine spherulitic carbonates where microbial organic molecules abound (Bischoff et al., 2020; Mercedes-Martín et al., 2021).

In summary, direct comparisons between fossil textures and the calcite crystals obtained in experiments can not only provide a qualitative assessment of the crystals formed but also a *quantitative* evaluation of the chemical parameters likely involved in the production of specific calcite morphologies. The combination of calcite growth form diagrams with data on metal partitioning and isotope fractionation (*sensu* Harouaka et al., 2016; Mavromatis et al., 2017) can potentially aid in the discrimination of calcites originated by abiotic or organomineralisation processes in recent and ancient carbonate precipitating settings.

5. CONCLUSIONS

1) A new calcite growth-form diagram for non-marine calcite precipitates was produced using tightly controlled synthetic alkaline and saline solutions designed to be similar to natural waters (Figure 4). This diagram shows that calcite morphologies nucleated under the

competing influence of a chemical ‘driving force’ (calcite saturation index) and the degree of interference with crystal growth by a microbial-derived organic additive (alginic acid).

2) Specific hydrogeochemical regions could be identified in the diagram in which particular calcite morphotypes formed, e.g., tetragonal calcite trapezohedrons, trigonal to tetragonal elongated prisms, calcite floating precipitates, spherulitic grains, double-terminated dumbbell fibro-radial particles, vertical spheroidal aggregates.

3) Lower calcite supersaturation conditions are prone to form single-crystal prismatic to dipyrnid calcite precipitates, while higher calcite supersaturation conditions tend to produce polycrystalline calcite spherulitic grains and their aggregates. Increasing contents in alginic acid contributed to the formation of curved and poorly faceted crystal morphologies with higher sphericity. Higher biopolymer concentrations led to the formation of conspicuous alginic hydrogels that correlate with the enhanced development of vertically-stacked spherulitic calcite particles. This indicates that alginic acid exhibits a pH-dependent behaviour over the stereochemical architecture of the polymer impacting crystal architecture and the arrangement of crystal aggregates.

4) Development of floating calcite rafts at the air-water interface was inhibited with rising alginic acids confirming that the physical location of crystallisation is generally modified by the presence of extracellular polymers, inhibiting degassing-forced precipitation.

5) Direct comparison between fossil freshwater material and the calcite crystal variation shown in *binary* morphology diagrams will enable a qualitative but also a quantitative assessment of

the chemical parameters likely to be involved in calcite morphogenesis. Addition of further physico-chemical parameters (flow velocity, concentration of sulphate, phosphate, sodium chloride, evaporation degree, organic molecules, trace element concentration, or time) may help to construct a more complex *ternary* (even poly-dimensional) morphology diagram for terrestrial carbonate precipitates, which will be more robust to the natural variability of real world' systems.

6) We offer growth-form phase diagrams as an unambiguous, quantifiable, and reproducible framework to help link processes with carbonate products in terrestrial carbonate settings (lakes, hot-springs, caves, rivers, soils). These diagrams can be used to organise, relate, and understand calcite petrographies while facilitating sedimentological and paleoclimatological analyses.

ACKNOWLEDGEMENTS

We are grateful to BP Exploration Co. (Grant reference: GPTL/BPX/MB/NB/89573) for permission to publish this manuscript delayed for publication due to confidentiality issues since May 2017. We warmly give thanks to many colleagues at BP's Carbonate Centre of Expertise (UK) for fruitful discussions on continental and 'Pre-salt' carbonates. We are indebted to Ian Billing, who recently died, for supporting this project and his encouragement towards developing experimental approaches to understand the formation of carbonate reservoir textures. Tony Sinclair, Bob Knight and Dr. Jorg Hardege (University of Hull) are kindly thanked for technical support. JR thanks the College of Petroleum Engineering & Geosciences for additional support. Prof. Adrian Immenhauser is thanked for his constructive criticism on an early draft. We are grateful for the comprehensive and useful reviews which

greatly improved the final version of the manuscript. Mariette Wolthers is acknowledged for her editorial assistance.

REFERENCES

Addadi, L., Raz, S., and Weiner, S. (2003). Taking advantage of disorder: amorphous calcium carbonate and its roles in biomineralization. *Advanced Materials* 15(12), 959-970.

Aizenberg, J., Addadi, L., Weiner, S. and Lambert, G. (1996). Stabilization of amorphous calcium carbonate by specialized macromolecules in biological and synthetic precipitates. *Advanced Materials* 8(3), 222-226.

Andrews, J.E. (2006). Palaeoclimatic records from stable isotopes in riverine tufas: Synthesis and review. *Earth-Science Reviews* 75(1-4), 85-104.

Andrews, J.E. and Brasier, A.T. (2005). Seasonal records of climatic change in annually laminated tufas: short review and future prospects. *Journal of Quaternary Science* 20(5), 411-421.

Arenas, C., Vázquez-Urbez, M., Auqué, L., Sancho, C., Osácar, C., and Pardo, G. (2014). Intrinsic and extrinsic controls of spatial and temporal variations in modern fluvial tufa

sedimentation: A thirteen-year record from a semi-arid environment. *Sedimentology* 61(1), 90–132.

Baas, J. H., Best, J. L., and Peakall, J. (2016). Predicting bedforms and primary current stratification in cohesive mixtures of mud and sand. *Journal of the Geological Society* 173(1), 12-45.

Bastianini, L., Rogerson, M., Mercedes-Martín, R., Prior, T. J., Cesar, E. A., & Mayes, W. M. (2019). What Causes Carbonates to Form “Shrubby” Morphologies? An Anthropocene Limestone Case Study. *Frontiers in Earth Science* 7, 1–19.

Bischoff, K., Sirantoine, E., Wilson, M. E., George, A. D., Mendes Monteiro, J., and Saunders, M. (2020). Spherulitic microbialites from modern hypersaline lakes, Rottneest Island, Western Australia. *Geobiology*, 18(6), 725-741.

Boch, R., Dietzel, M., Reichl, P., Leis, A., Baldermann, A., Mittermayr, F., and Pölt, P. (2015). Rapid ikaite ($\text{CaCO}_3 \cdot 6\text{H}_2\text{O}$) crystallization in a man-made river bed: hydrogeochemical monitoring of a rarely documented mineral formation. *Applied Geochemistry* 63, 366-379.

Boch, R., Leis, A., Haslinger, E., Goldbrunner, J. E., Mittermayr, F., Fröschl, H., and Dietzel, M. (2017). Scale-fragment formation impairing geothermal energy production: interacting H₂S corrosion and CaCO₃ crystal growth. *Geothermal Energy* 5(1), 1-19

Boch, R., Wang, X., Kluge, T., Leis, A., Lin, K., Pluch, H., and Dietzel, M. (2019). Aragonite–calcite veins of the ‘Erzberg’ iron ore deposit (Austria): Environmental implications from young fractures. *Sedimentology* 66(2), 604-635.

Bonny, S., and Jones, B. (2003). Microbes and mineral precipitation, Miette Hot Springs, Jasper National Park, Alberta, Canada. *Canadian Journal of Earth Sciences* 40(11), 1483-1500.

Braissant, O., Cailleau, G., Dupraz, C. and Verrecchia, E.P. (2003) Bacterially induced mineralization of calcium carbonate in terrestrial environments: the role of exopolysaccharides and amino acids. *Journal of Sedimentary Research* 73, 485-490.

Capezzuoli, E., Gandin, A., and Pedley, M. (2014). Decoding tufa and travertine (fresh water carbonates) in the sedimentary record: The state of the art. *Sedimentology* 61(1), 1-21.

Ceraldi, T. S., and Green, D. (2017). Evolution of the South Atlantic lacustrine deposits in response to Early Cretaceous rifting, subsidence and lake hydrology. *Geological Society, London, Special Publications* 438(1), 77-98.

Chafetz, H. S., and Buczynski, C. (1992). Bacterially induced lithification of microbial mats. *Palaios*, 7 (3): 277-293.

Chafetz, H. S., and Guidry, S. A. (1999). Bacterial shrubs, crystal shrubs, and ray-crystal shrubs: bacterial vs. abiotic precipitation. *Sedimentary Geology* 126(1-4), 57-74.

Chekroun, K. B., Rodríguez-Navarro, C., González-Muñoz, M. T., Arias, J. M., Cultrone, G., and Rodríguez-Gallego, M. (2004). Precipitation and growth morphology of calcium carbonate induced by *Myxococcus xanthus*: implications for recognition of bacterial carbonates. *Journal of Sedimentary Research* 74(6), 868-876.

Cölfen, H., and Antonietti, M. (2008). Mesocrystals and nonclassical crystallization. John Wiley & Sons.

Cölfen, H., and Qi, L. (2001). A systematic examination of the morphogenesis of calcium carbonate in the presence of a double-hydrophilic block copolymer. *Chemistry - A European Journal* 7(1), 106–116.

Connell, T.L. and Dreiss, S.J. (1995). Chemical evolution of shallow groundwater along the northeast shore of Mono Lake, California. *Water Resources Research* 31(12), 3171-3182.

Daliran, F. (2008). The carbonate rock-hosted epithermal gold deposit of Agdarreh, Takab geothermal field, NW Iran—hydrothermal alteration and mineralisation. *Mineralium Deposita* 43(4), 383-404.

Défarge, C. (2006). Organomineralization. *Encyclopedia of Geobiology* 4(2), 697–701.

Erthal, M. M., Capezzuoli, E., Mancini, A., Claes, H., Soete, J., and Swennen, R. (2017). Shrub morpho-types as indicator for the water flow energy-Tivoli travertine case (Central Italy). *Sedimentary Geology* 347, 79-99.

Frisia, S., Borsato, A., Fairchild, I.J. and McDermott, F. (2000). Calcite Fabrics, Growth Mechanisms, and Environments of Formation in Speleothems from the Italian Alps and Southwestern Ireland. *Journal of Sedimentary Research* 70(5), 1183-1196.

Gomes, H. I., Rogerson, M., Burke, I. T., Stewart, D. I., & Mayes, W. M. (2017). Hydraulic and biotic impacts on neutralisation of high-pH waters. *Science of the Total Environment* 601, 1271-1279.

Grassmann, O., Neder, R. B., Putnis, A., and Löbmann, P. (2003). Biomimetic control of crystal assembly by growth in an organic hydrogel network. *American Mineralogist* 88(4), 647–652. <https://doi.org/10.2138/am-2003-0418>

Han, Y.J., Wysocki, L.M., Thanawala, M.S., Siegrist, T. and Aizenberg, J. (2005). Template-dependent morphogenesis of oriented calcite crystals in the presence of magnesium ions. *Angewandte Chemie International Edition* 44(16), 2386- 2390.

Harms, J. C., Southard, J. B., and Walker, R. G. (1982). Structures and Sequences in Clastic Rocks. SEPM Short Course Notes 9. *Society of Economic Paleontologists and Mineralogists*, 9. <https://doi.org/10.2110/scn.82.09>

Herlinger, R., Zambonato, E. E., & Ros, L. F. D. E. (2017). Influence of diagenesis on the quality of Lower Cretaceous Pre-Salt lacustrine carbonate reservoirs from Northern Campos Basin, Offshore Brazil. *Journal of Sedimentary Research* 87(12), 1285–1313.

Harouaka, K., Mansor, M., Macalady, J. L., and Fantle, M. S. (2016). Calcium isotopic fractionation in microbially mediated gypsum precipitates. *Geochimica et Cosmochimica Acta* 184, 114–131. <https://doi.org/10.1016/j.gca.2016.03.003>

Haug, A., Larsen, B., and Smidsrød, O. (1974). Uronic acid sequence in alginate from different sources. *Carbohydrate Research*, 32(2), 217-225.

Imai, H., (2016). Mesostructured crystals: Growth processes and features. *Progress in Crystal Growth and Characterization of Materials* 62 (2), 212-226.

Jones, B. (1994). Diagenetic processes associated with plant roots and microorganisms in karst terrains of the Cayman Islands, British West Indies. *Developments in Sedimentology* 51, 425-475.

Jones, B. (2017). Review of aragonite and calcite crystal morphogenesis in thermal spring systems. *Sedimentary Geology* 354, 9-23.

Jones, B., and Peng, X. (2014). Signatures of biologically influenced CaCO₃ and Mg-Fe silicate precipitation in hot springs: Case study from the Ruidian geothermal area, western Yunnan Province, China. *Sedimentology* 61(1), 56-89.

Jones, B., and Renaut, R. W. (1995). Noncrystallographic calcite dendrites from hot-spring deposits at Lake Bogoria, Kenya. *Journal of Sedimentary Research*, 65(1a): 154-169.

Kim, Y.-Y., Freeman, C. L., Gong, X., Levenstein, M. A., Wang, Y., Kulak, A., Meldrum, F. C. (2017). The Effect of Additives on the Early Stages of Growth of Calcite Single Crystals. *Angewandte Chemie International Edition* 200444, 11885–11890.
<https://doi.org/10.1002/anie.201706800>

Kloareg, B., and Quatrano, R. S. (1988). Structure of the cell walls of marine algae and ecophysiological functions of the matrix polysaccharides. *Oceanography and Marine Biology: An Annual Review* 26, 259-315.

Kosanović, C., Fermani, S., Falini, G., and Kralj, D. (2017). Crystallization of Calcium Carbonate in Alginate and Xanthan Hydrogels. *Crystals* 7(12), 355.

Lapotre, M. G., Lamb, M. P., and McElroy, B. (2017). What sets the size of current ripples?. *Geology* 45 (3), 243- 246.

Li, L., Fang, Y., Vreeker, R., Appelqvist, I., and Mendes, E. (2007). Reexamining the egg-box model in calcium– alginate gels with X-ray diffraction. *Biomacromolecules* 8(2), 464-468.

Ma, Y., and Feng, Q. (2011). Alginate hydrogel-mediated crystallization of calcium carbonate. *Journal of Solid State Chemistry* 184(5), 1008-1015.

Mao, Z., and Huang, J. (2007). Habit modification of calcium carbonate in the presence of malic acid. *Journal of Solid State Chemistry* 180(2), 453–460.

<https://doi.org/10.1016/j.jssc.2006.11.002>

Mavromatis, V., Immenhauser, A., Buhl, D., Purgstaller, B., Baldermann, A., and Dietzel, M. (2017). Effect of organic ligands on Mg partitioning and Mg isotope fractionation during low-temperature precipitation of calcite in the absence of growth rate effects. *Geochimica et Cosmochimica Acta*, 207 139–153. <https://doi.org/10.1016/j.gca.2017.03.020>

McCormack, J., Nehrke, G., Jöns, N., Immenhauser, A., and Kwiecien, O. (2019). Refining the interpretation of lacustrine carbonate isotope records: Implications of a mineralogy-specific Lake Van case study. *Chemical Geology* 513, 167-183.

Meldrum, F.C. and Cölfen, H. (2008). Controlling Mineral Morphologies and Structures in Biological and Synthetic Systems. *Chemical Reviews* 108(11), 4332-4432.

Mercedes-Martín, R., Rogerson, M.R., Brasier, A.T., Vonhof, H.B., Prior, T.J., Fellows, S.M., Reijmer, J.J.G., Billing, I. and Pedley, H.M. (2016). Growing spherulitic calcite grains

in saline, hyperalkaline lakes: experimental evaluation of the effects of Mg-clays and organic acids. *Sedimentary Geology* 335, 93-102.

Mercedes-Martín, R., Brasier, A. T., Rogerson, M., Reijmer, J. J., Vonhof, H., and Pedley, M. (2017). A depositional model for spherulitic carbonates associated with alkaline, volcanic lakes. *Marine and Petroleum Geology* 86, 168-191.

Mercedes-Martín, R., Ayora, C., Tritlla, J., Sánchez-Román, M. (2019). The hydrochemical evolution of alkaline volcanic lakes: a model to understand the South Atlantic Pre-salt mineral assemblages. *Earth-Science Reviews* 198, 102938.

Mercedes-Martín, R., Rao, A., Rogerson, M., Sánchez-Román, M. (2021). Effects of Salinity, Organic Acids and Alkalinity in the Growth of Calcite Spherulites: Implications for Evaporitic Lacustrine Sedimentation. *The Depositional Record*). <https://doi.org/10.1002/dep2.136>

Meyer, M., Aldenderfer, M., Wang, Z., Hoffmann, D., Dahl, J., Degering, D., Haas, W. and Schlütz, F. (2017). Permanent human occupation of the central Tibetan Plateau in the early Holocene. *Science* 355(6320) 64-67.

Montanari, G., Lakshatanov, L. Z., Tobler, D. J., Dideriksen, K., Dalby, K. N., Bovet, N., & Stipp, S. L. S. (2016). Effect of Aspartic Acid and Glycine on Calcite Growth. *Crystal Growth and Design* 16(9), 4813–4821. <https://doi.org/10.1021/acs.cgd.5b01635>

Morse, J. W., Arvidson, R. S., and Lüttge, A. (2007). Calcium carbonate formation and dissolution. *Chemical Reviews* 107 (2), 342-381.

Oaki, Y., and Imai, H. (2003). Experimental Demonstration for the Morphological Evolution of Crystals Grown in Gel Media. *Crystal Growth & Design* 3(5), 711-716.

Orme, C. A., Noy, A., Wierzbicki, A., McBride, M. T., Grantham, M., Teng, H. H., Dove, P. M. and DeYoreo, J. J. (2001). Formation of chiral morphologies through selective binding of amino acids to calcite surface steps. *Nature* 411(6839), 775-779.

Pedley, M. (2014). The morphology and function of thrombotic calcite precipitating biofilms: A universal model derived from freshwater mesocosm experiments. *Sedimentology* 61(1), 22-40.

Pedley, H. M., and Rogerson, M. (2010). In vitro investigations of the impact of different temperature and flow velocity conditions on tufa microfabric. *Geological Society, London, Special Publications* 336(1), 193-210.

Pedley, H.M., Rogerson, M. and Middleton, R. (2009). The growth and morphology of freshwater calcite precipitates from in vitro mesocosm flume experiments; the case for biomediation. *Sedimentology* 56, 511-527.

Pentecost, A. (2005). *Travertine*. Springer Science & Business Media.

Perry IV, T. D., Cygan, R. T., and Mitchell, R. (2006). Molecular models of alginic acid: Interactions with calcium ions and calcite surfaces. *Geochimica et Cosmochimica Acta* 70(14), 3508-3532.

Rainey, D. K., and Jones, B. (2009). Abiotic versus biotic controls on the development of the Fairmont Hot Springs carbonate deposit, British Columbia, Canada. *Sedimentology* 56(6), 1832-1857.

Rao, A., Vásquez-Quitral, P., Fernández, M. S., Berg, J. K., Sánchez, M., Drechsler, M., Neira-Carillo, A., Arias, J. L., Gebauer, D. and Cölfen, H. (2016). pH-dependent schemes of calcium carbonate formation in the presence of alginates. *Crystal Growth & Design* 16(3), 1349-1359.

Reddy, M. M., and Hoch, A. (2012). Calcium carbonate nucleation in an alkaline lake surface water, Pyramid Lake, Nevada, USA. *Aquatic Geochemistry* 18(2), 95-113.

Regenspurg, S., Feldbusch, E., Byrne, J., Deon, F., Driba, D. L., Henniges, J., and Schubert, C. (2015). Mineral precipitation during production of geothermal fluid from a Permian Rotliegend reservoir. *Geothermics* 54, 122-135.

Renaut, R. W., Owen, R. B., Jones, B., Tiercelin, J. J., Tarits, C., Ego, J. K., and Konhauser, K. O. (2013). Impact of lake-level changes on the formation of thermogene travertine in continental rifts: Evidence from Lake Bogoria, Kenya Rift Valley. *Sedimentology* 60(2), 428-468.

Rivadeneira, M. A., Martín-Algarra, A., Sánchez-Román, M., Sánchez-Navas, A., and Martín-Ramos, J. D. (2010). Amorphous Ca-phosphate precursors for Ca-carbonate biominerals mediated by *Chromohalobacter marismortui*. *The ISME Journal* 4(7), 922–932. <https://doi.org/10.1038/ismej.2010.17>

Rogerson, M., Mercedes-Martín, R., Brasier, A. T., McGill, R. A., Prior, T. J., Vonhof, H., Fellows, S. M., Reijmer, J. J. G., McClymont, E., Billing, I., Matthews, A., Pedley, M. (2017). Are spherulitic lacustrine carbonates an expression of large-scale mineral carbonation? A case study from the East Kirkton Limestone, Scotland. *Gondwana Research* 48, 101-109.

Rogerson, M., Pedley, H. M., Wadhawan, J. D., and Middleton, R. (2008). New insights into biological influence on the geochemistry of freshwater carbonate deposits. *Geochimica et Cosmochimica Acta* 72(20), 4976-4987.

Saller, A., Rushton, S., Buambua, L., Inman, K., McNeil, R., and Dickson, J. T. (2016). Presalt stratigraphy and depositional systems in the Kwanza Basin, offshore Angola. *AAPG Bulletin* 100(7), 1135-1164.

Seto, J. (Ed.). (2012). Advanced topics in biomineralization. BoD–Books on Demand.

Saunders, P., Rogerson, M., Wadhawan, J. D., Greenway, G., and Pedley, H. M. (2014). Mg/Ca ratios in freshwater microbial carbonates: Thermodynamic, kinetic and vital effects. *Geochimica et Cosmochimica Acta* 147, 107-118.

Schindler, R.J., Parsons, D.R., Ye, L., Hope, J.A., Baas, J.H., Peakall, J., Manning, A.J., Aspden, R.J., Malarkey, J. and Simmons, S. (2015). Sticky stuff: Redefining bedform prediction in modern and ancient environments. *Geology* 43(5), 399-402.

Schneider J. (1977) Carbonate Construction and Decomposition by Epilithic and Endolithic Micro-organisms in Salt- and Freshwater. In: Flügel E. (eds) *Fossil Algae*. Springer, Berlin, Heidelberg. https://doi.org/10.1007/978-3-642-66516-5_27.

Smith, J.R., Hawkins, A.L., Asmerom, Y., Polyak, V. and Giegengack, R. (2007). New age constraints on the Middle Stone Age occupations of Kharga Oasis, Western Desert, Egypt. *Journal of Human Evolution* 52(6), 690-701.

Song, R. Q., and Cölfen, H. (2011). Additive controlled crystallization. *CrystEngComm*, 13(5), 1249-1276.

Southard, J. B., and Boguchwal, L. A. (1990). Bed configurations in steady unidirectional water flows. Part 2. Synthesis of flume data. *Journal of Sedimentary Research* 60(5): 658-679.

Stow, D. A. V., Hernández-Molina, F. J., Llave, E., Bruno, M., García, M., del Rio, V. D., Somoza, L. and Brackenridge, R. E. (2013). The Cadiz Contourite Channel: Sandy contourites, bedforms and dynamic current interaction. *Marine Geology* 343, 99-114.

Sun, W., Jayaraman, S., Chen, W., Persson, K.A. and Ceder, G. (2015) Nucleation of metastable aragonite CaCO₃ in seawater. *Proceedings of the National Academy of Sciences* 112(11), 3199-3204.

Sunagawa, I. (2005). Crystals: growth, morphology, and perfection. *Cambridge University Press*. 295pp.

Taylor, M. P., Drysdale, R. N., and Carthew, K. D. (2004). The formation and environmental significance of calcite rafts in tropical tufa-depositing rivers of northern Australia. *Sedimentology* 51(5), 1089-1101.

Terra et al., (2010). Classificação de rochas carbonáticas aplicável às bacias sedimentares brasileiras. *Bulletin Geoscience Petrobras, Rio de Janeiro* 18 (1), 9-29.

Trichet, J., and Défarge, C., (1995). Non-biologically supported organomineralization. In Allemand, D., and Cuif, J. P. (eds.), Proceedings 7th International Symposium on Biomineralization. Bulletin de l'Institut Océanographique de Monaco, n° spéc. 14, Vol. 2, 203–236.

van den Berg J.H., van Gelder A. (1993). A new bedform stability diagram, with emphasis on the transition of ripples to plane bed in flows over fine sand and silt. In: Marzo M., Puigdefabregas C. (eds) *Alluvial Sedimentation. International Association of Sedimentologists, Special Publications* 17, 11–21.

Wright, V.P. (2012). Lacustrine carbonates in rift settings: the interaction of volcanic and microbial processes on carbonate deposition. *Geological Society, London, Special Publications* 370(1), 39-47.

Young, J. R., Davis, S. A., Bown, P. R., and Mann, S. (1999). Coccolith ultrastructure and biomineralisation. *Journal of Structural Biology* 126(3), 195-215.

Zhang, G., Morales, J., & Garcia-Ruiz, J. M. (2017). Growth behaviour of silica/carbonate nanocrystalline composites of calcite and aragonite, 5, 1658. *Journal of Materials Chemistry* 1658–1663. <https://doi.org/10.1039/C6TB02612E>

Zhou, L., and O'Brien, P. (2008). Mesocrystals: a new class of solid materials. *Small* 4(10), 1566-1574.

FIGURE CAPTIONS :

FIGURE 1. Diagram of the characteristic experimental calcite morphotypes (shown as SEM photomicrographs) formed in association to specific calcite saturation indices (SI) and alginic acid contents.

FIGURE 2. Summary of calcite growth form nomenclature and crystal distribution recognised in experiments.

FIGURE 3. Dominant growth forms and patterns of distribution of benthic and floating crystals formed under the influence of saturation index (SI) and alginic acid concentrations.

FIGURE 4. **A)** Petrographic domains established on the basis of the dominant microscopic calcite assemblages produced under the competing influence of saturation index (SI) and alginic acid concentrations. See Figure 2 for crystal terminology. **B)** Summary of calcite crystal domains. **C)** Sketch showing the domains for ‘abiotic precipitation’ (3, 5 and 7) and ‘organomineralisation’ (2, 4, 6, 7 and 8).

FIGURE 5. ‘Surface crystal crusts’. **A-B)** Complex mineral mixtures of calcium carbonate, sodium chloride and amorphous silicate-like phases precipitated as benthic crystals forming patchy layers. **B)** Detail of such mixtures showing heterogeneous aggregates. **C)** Acicular calcite fan bodies interfering each other and growing from circular bands. **D)** Detail of C showing the fibrous, elongated components. **E)** Banded calcite overgrowths producing individual structureless and circular calcite crystals (note two orientations of the same crystal type). **F)** Linear banded calcite overgrowths can contain euhedral halite cubic crystals (hal). Saturation index and alginic contents are annotated on top, and coloured circle refers to Fig. 4A and 4B. Numbers refer to crystal terminology attached to the bottom side. Yellow asterisks indicate EDS measurement points.

FIGURE 6. ‘Elongated prisms’ and ‘Di-pyramids’ crystals. **A)** Double-terminated trigonal to tetragonal elongated prismatic calcite crystals some of them twinned (tw). **B)** A lower layer made up of tightly fitted, small double-terminated tetragonal elongated prismatic and tetragonal calcite crystals. A foreground upper layer of di-pyramid calcite crystal aggregates. **C)** Di-pyramids, truncated di-pyramids and tetragonal trapezohedrons growing as benthic precipitates. **D)** A dense lower layer of poorly defined and intertwined di-pyramid calcite crystals underlying bigger scale di-pyramid calcite crystals some of them with protruded and rounded corners. **E)** A lower layer made up of tiny rhombic calcite crystals underlying an upper layer of aggregated di-pyramids, tetragonal trapezohedrons and rose spheroidal calcite crystals. Dried alginic acid gels (Alg) are enveloping these crystals. **F)** A dense layer of dodecahedron calcite crystals. Saturation index and alginic contents are annotated on top, and coloured circle refers to domains in Fig. 4A and B. Numbers refer to crystal terminology attached to the bottom side. Yellow asterisks indicate EDS measurement points..

FIGURE 7. ‘Di-pyramid’, ‘Rhombic’ and ‘Dumbbell’ crystals. **A)** Di-pyramid calcite crystals some of them with protruded and rounded corners are found either as lower or upper layers. Dodecahedron calcite crystals are coating either benthic occurrences or floating rafts with flat surfaces (top left). **B)** Di-pyramid calcite crystals with protruded and rounded faces growing as lower layer precipitates forming densely fitted crusts. **C)** Densely packed, tiny rhombic calcite crystals forming crusts. Globular clusters (gc) can be formed on top of them. **D)** Dense lower layers of tetrahedron calcite crystals are covered by aggregated dumbbell spherules. **E)** Dense lower layers of tetrahedron calcite crystals are covered by aggregated dumbbell spherules which form vertically packed bodies. Dodecahedron coatings are present.

F) Floating rafts are made up of trigonal flat prismatic/faceted calcite crystals intertwined each other with random orientations (dotted yellow lines). Tetragonal prisms stack downward. Saturation index and alginic contents are annotated on top, and coloured circle refers to domains in Fig. 4A and B. Numbers refer to crystal terminology attached to the bottom side. Yellow asterisks indicate EDS measurement points.

FIGURE 8. ‘Spherical’ crystals. **A)** Fibro-radial calcite crystals are normally coated by dense and homogeneous layers of rhombic imbricated calcite crystals (inset). **B)** Fibro-radial crystals coated by tetrahedron calcite crystals. **C)** Fibro-radial calcite crystals coated by rhombic imbricated crystals and overlaid by dumbbell fibro-radial calcite spherules. **D)** Fibro-radial calcite spherules (inset) covered by rhombic imbricated crystals forming elongated bridges between aggregates spherules. Dumbbell fibro-radial calcite spherules also occur. **E)** Fibro-radial and dumbbell calcite spherules covered by reinforced rhombic calcite crystal coatings. **F)** Fibro-radial and dumbbell calcite spherules tend to aggregate forming globular clusters covered by rhombic imbricated calcite crystals. Saturation index and alginic contents are annotated on top, and coloured circle refers to domains in Fig. 4A and B. Numbers refer to crystal terminology attached to the bottom side. Yellow asterisks indicate EDS measurement points..

FIGURE 9. ‘Stacked spherical’ crystals. **A)** Enhanced aggregation of vertically growing di-pyramids to protruded di-pyramids produced ‘shrubby’ calcite clusters. **B)** Alginic acid (Alg) is enveloping fibro-radial spherules. Tiny dumbbell fibro-radial calcite spherules are also observed. **C)** Globular bunches growing laterally and vertically are made up of fibro-radial

and dumbbell fibro-radial calcite spherules. Rhombic calcite crystal coatings cover the precipitates. **D)** Enhanced vertical stacking of individual fibro-radial calcite spherules growing on top of each other. Floating rafts (top centre) are made up of fibro-radial calcite spherule clusters growing laterally. **E)** Floating rafts are made up of fibro-radial calcite spherules nucleated in the air-water interface. Agglutination of spherical calcite bodies is common. **F)** Aggregated bunches of fibro-radial calcite spherules and dumbbells forming discrete globular ‘shrubby’ bodies. Saturation index and alginic contents are annotated on top, and coloured circle refers to domains in Fig. 4A and B. Numbers refer to crystal terminology attached to the bottom side. Yellow asterisks indicate EDS measurement points.

TABLE 1. Composition of the initial synthetic parental solution.

TABLE 2. Hydrochemical parameters of the experimental runs. Cation concentrations (Ca, Mg, Na) and ionic strength are referred to the values after experiment termination. $\{Ca^{2+}\}$ and $\{CO_3^{2-}\}$ activities; $[Ca^{2+}]$ and $[Mg^{2+}]$ concentrations, Initial Total Alkalinity (TA_i), and Saturation Index (SI) are referred to the initial solutions. Saturation indexes, calcium and magnesium activities, ionic strengths, and Initial Total Alkalinities were obtained using PHREEQC modelling.

TABLE 3. Summary of mineralogies, abundance of floating, neck and benthic crystals, and hydrogels in the experiments.

TABLE 4. Average calcium and magnesium removal percentages in every experiment.

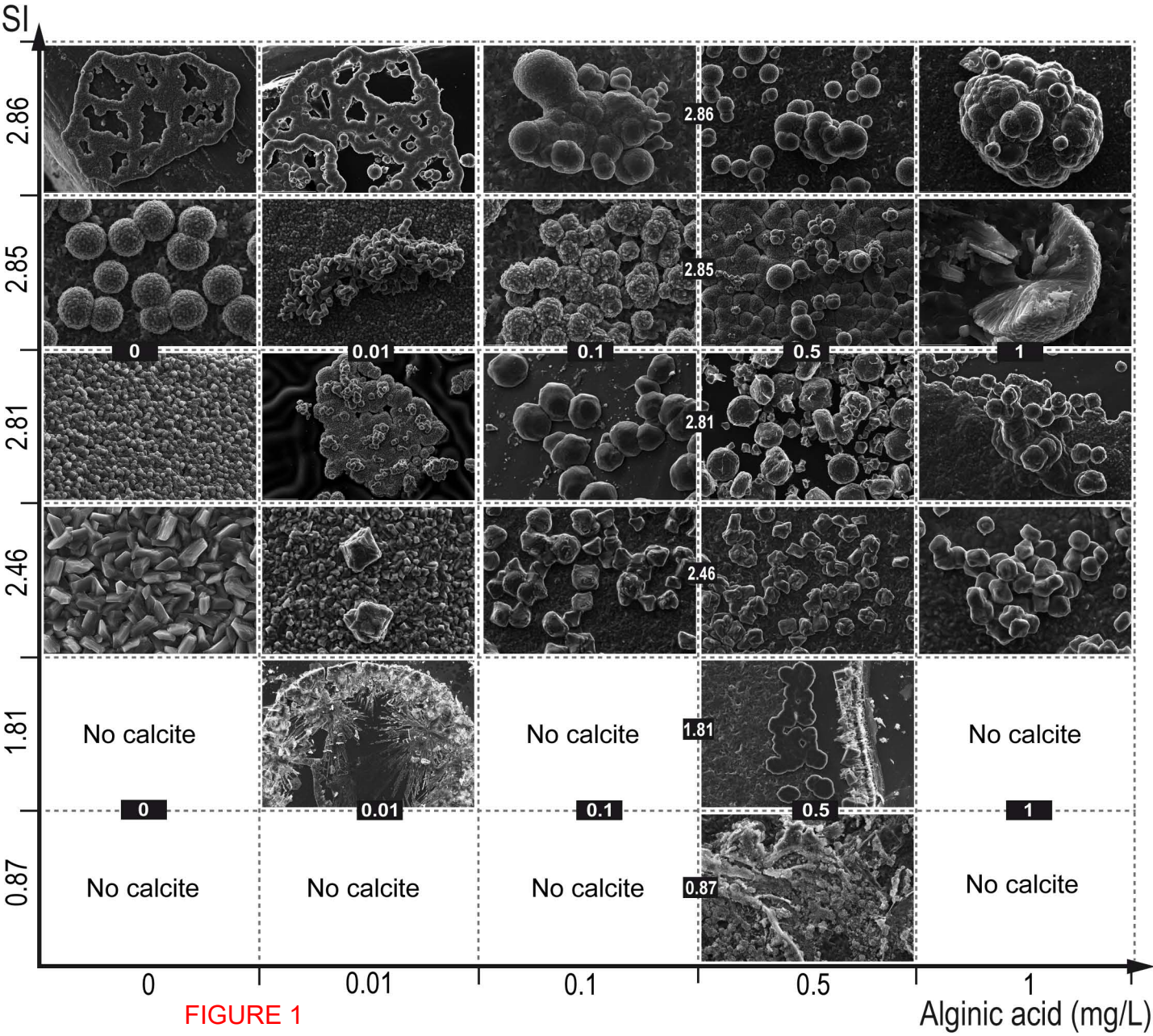
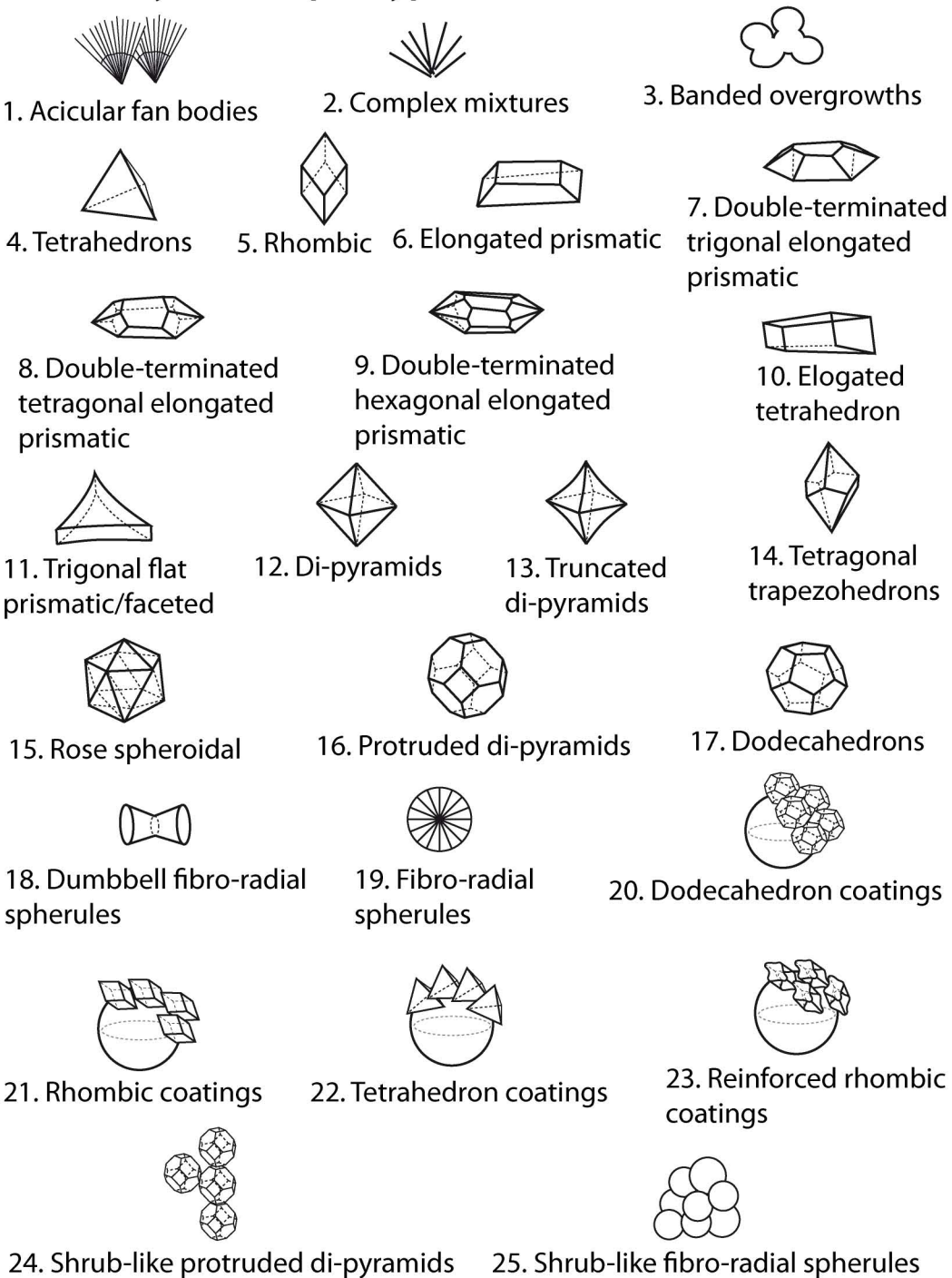


FIGURE 1

Alginate acid (mg/L)

Calcite crystal morphotypes



Crystal distribution

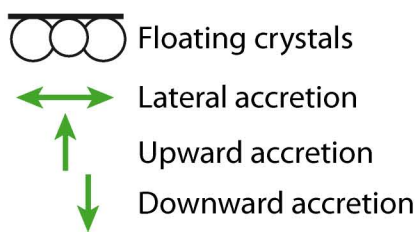


FIGURE 2

SI calcite

Crystals are not to scale

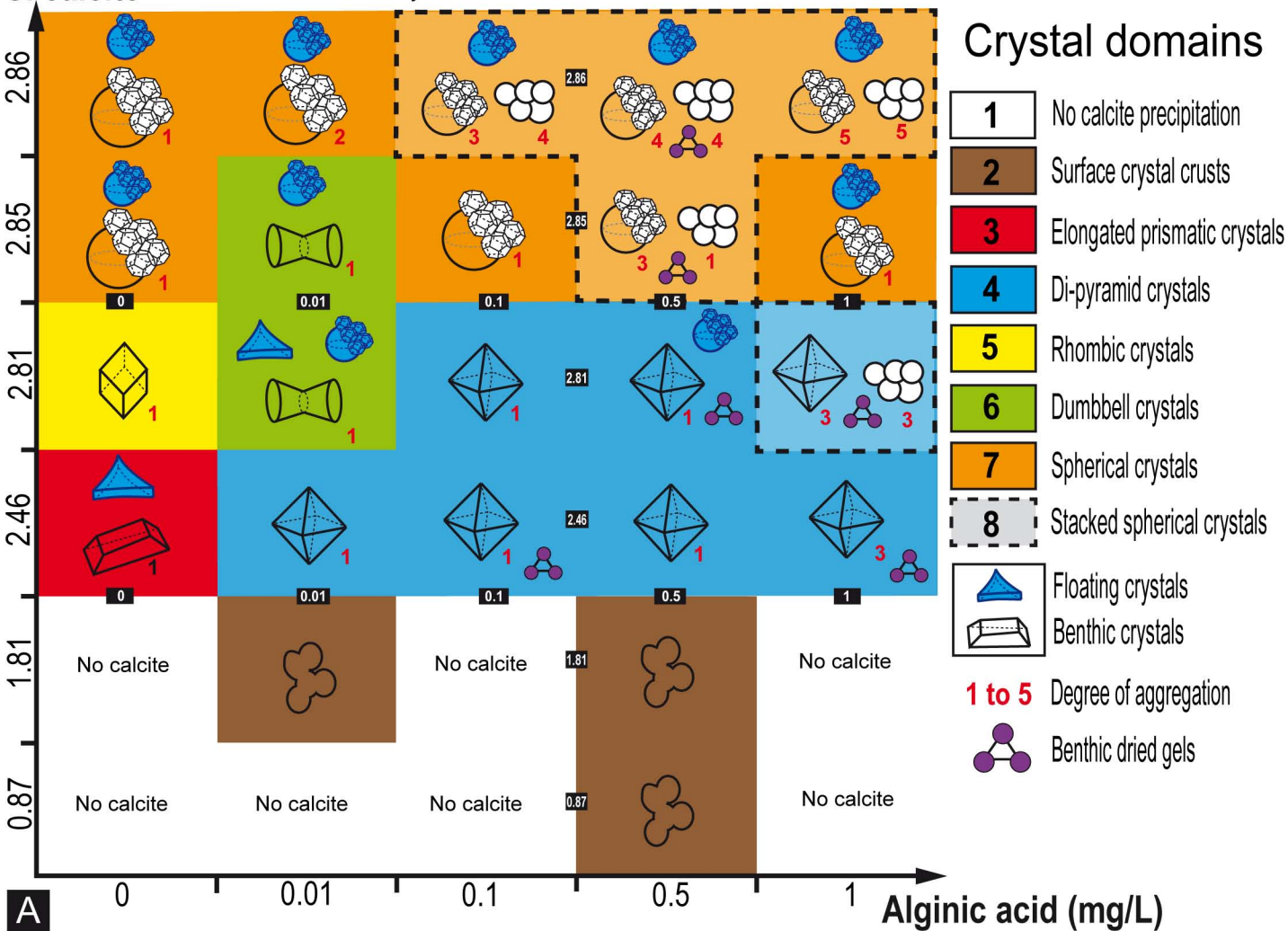
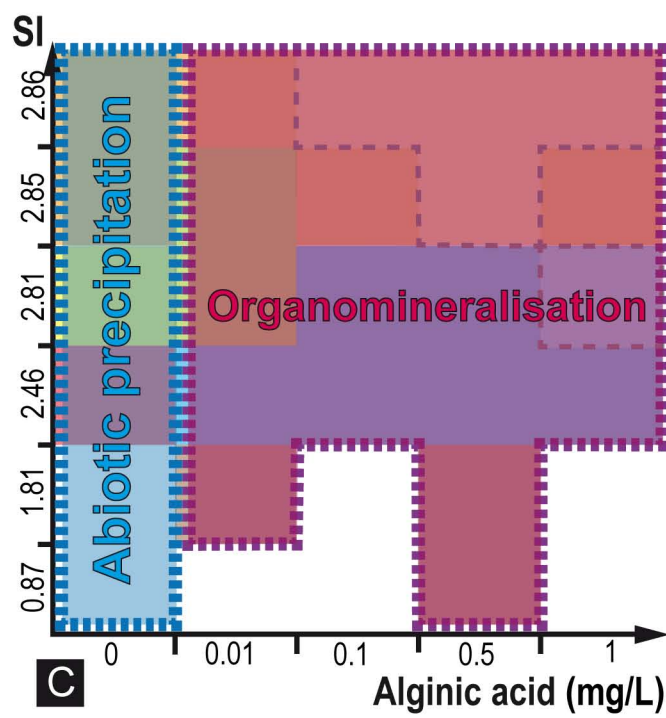
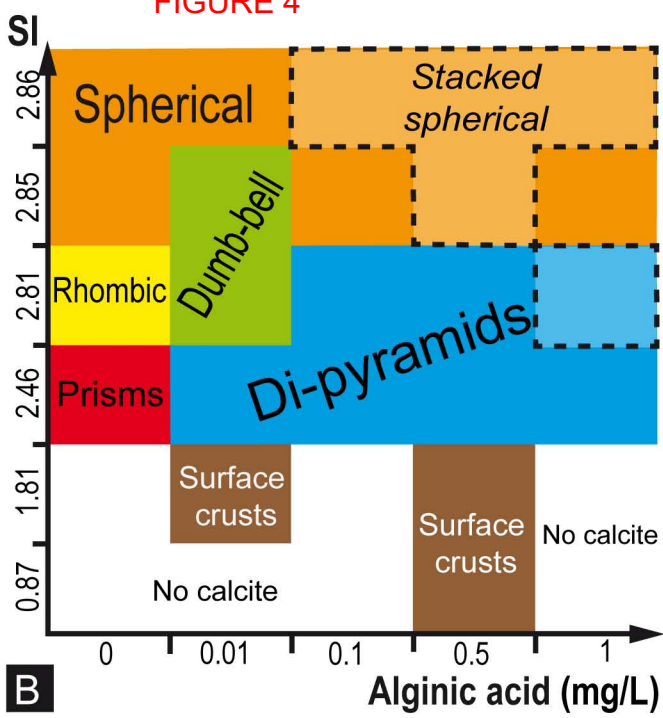


FIGURE 4



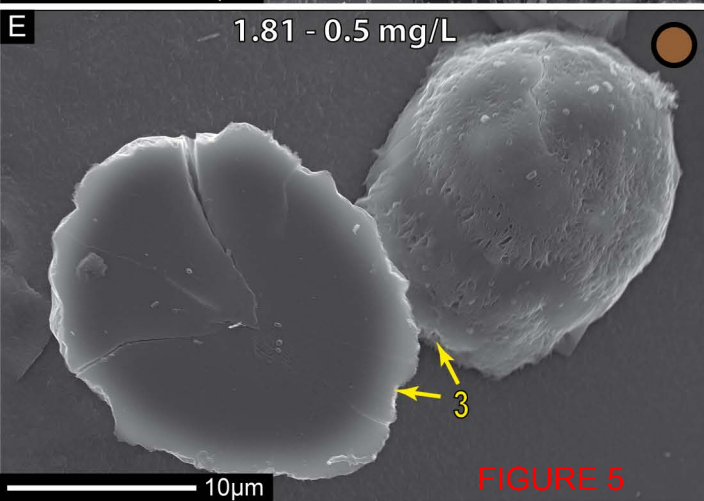
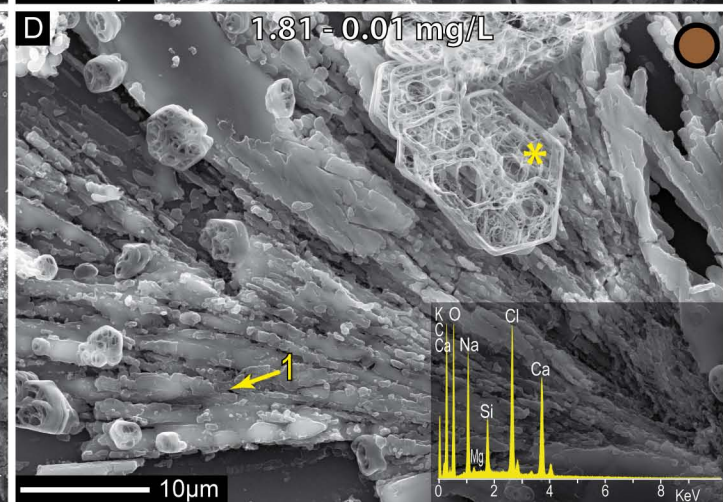
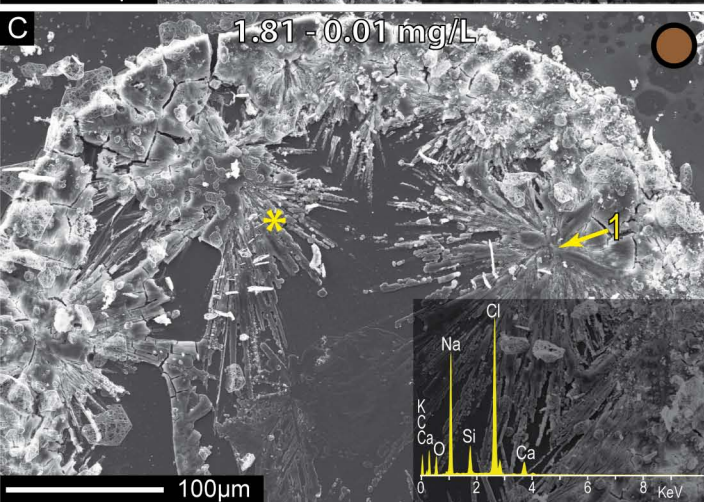
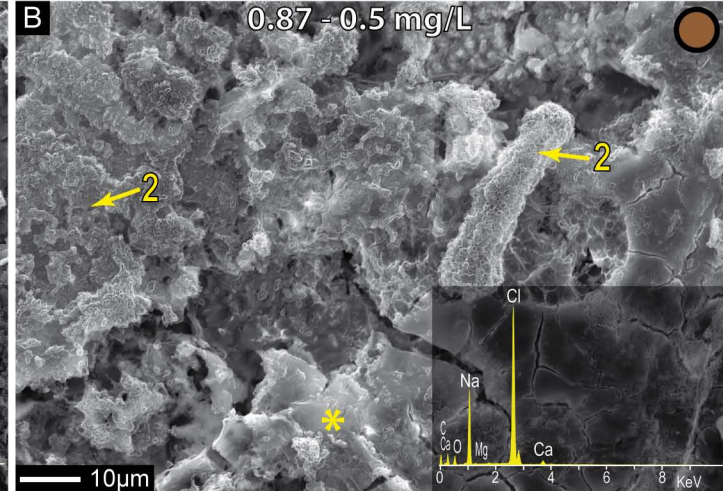
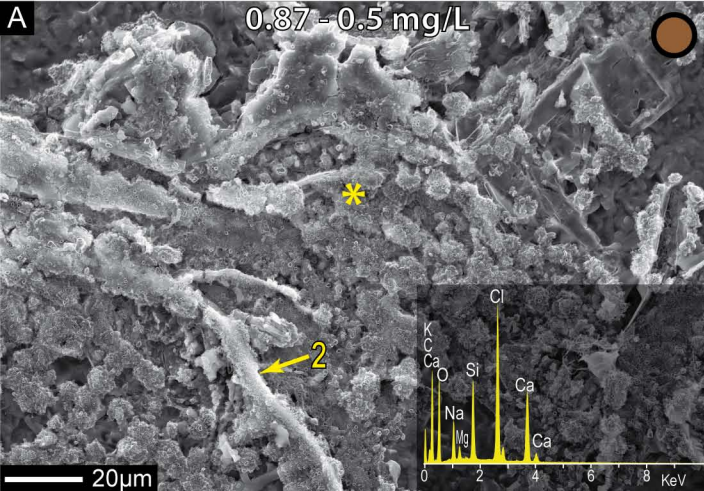



FIGURE 5

 1. Acicular fan bodies

 2. Complex mixtures

 3. Banded overgrowths

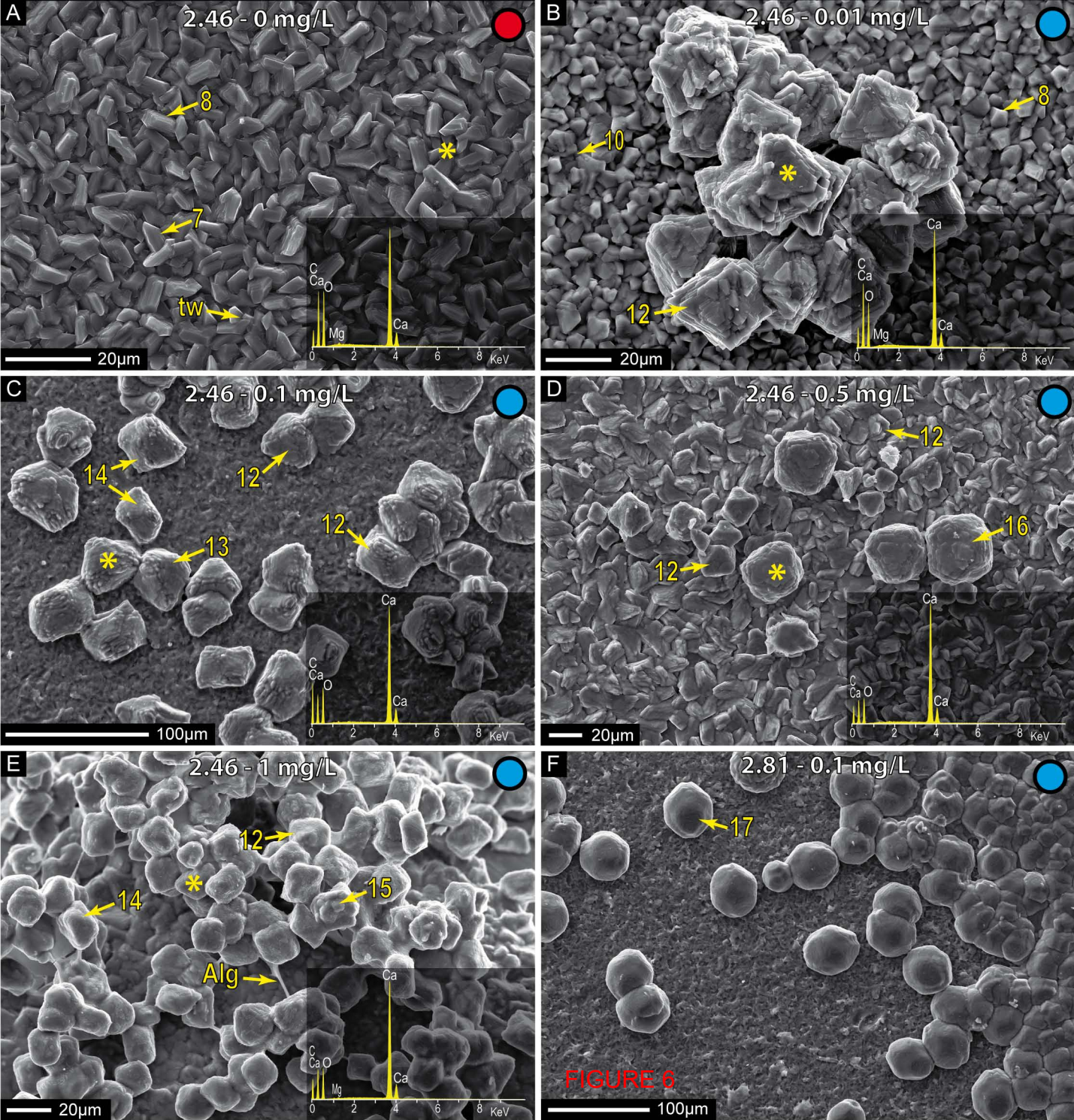


FIGURE 6

- 7. Double terminated trigonal elongated prismatic
- 8. Double terminated tetragonal elongated prismatic
- 9. Tetrahedrons
- 10. Tetrahedrons
- 11. Di-pyramids
- 12. Di-pyramids
- 13. Truncated di-pyramids
- 14. Tetragonal trapezohedrons
- 15. Rose spheroidal
- 16. Protruded di-pyramids
- 17. Dodecahedrons

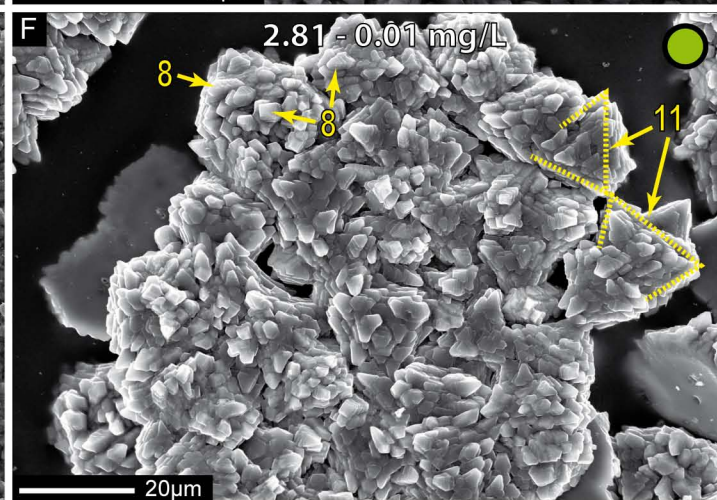
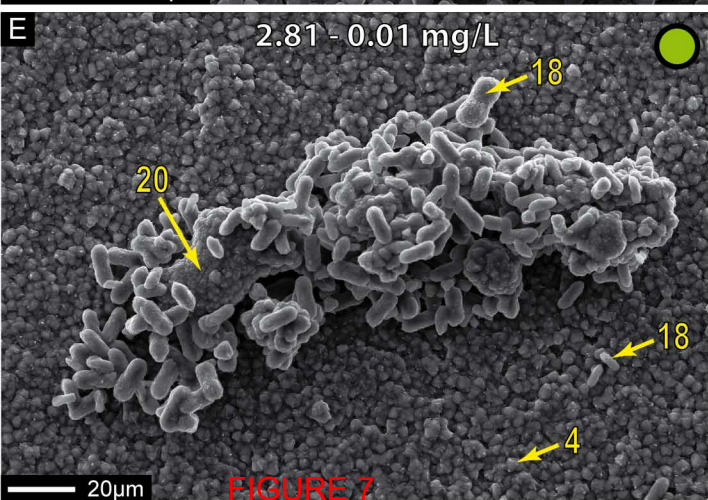
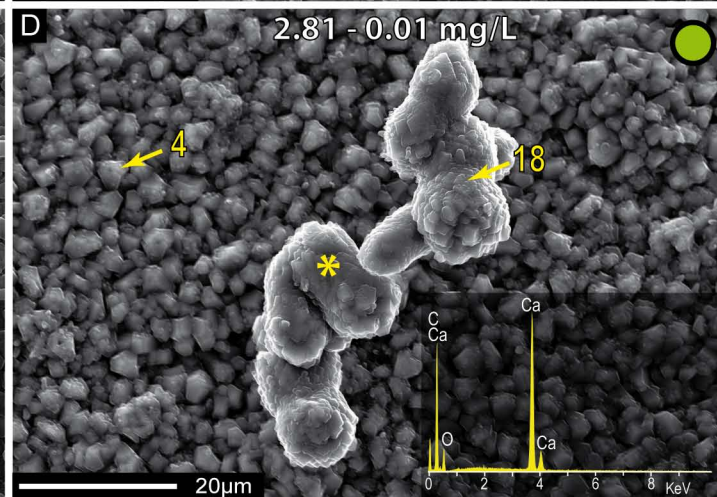
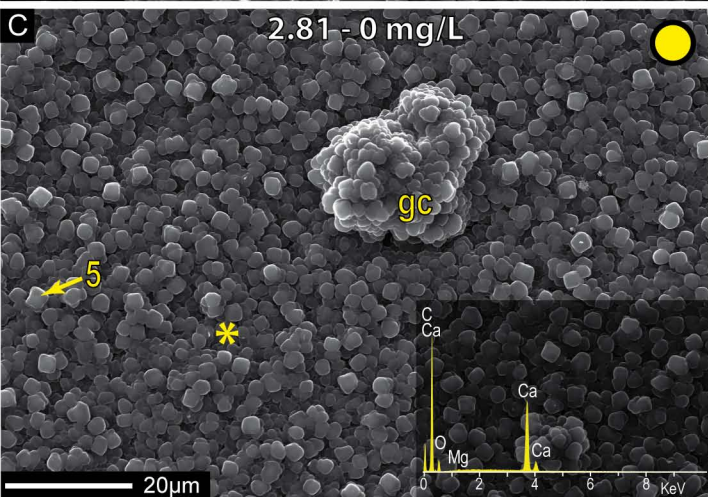
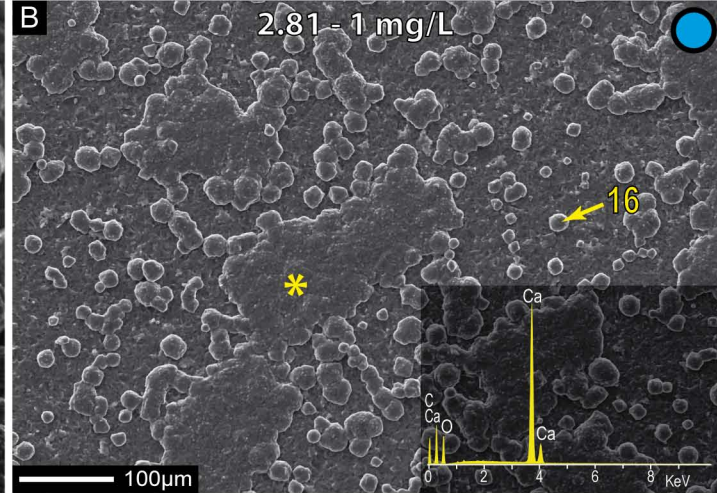
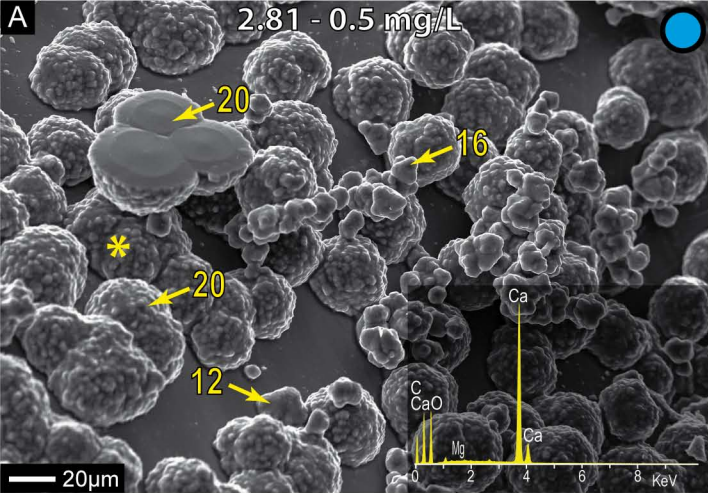


FIGURE 7

- 4. Tetrahedrons
- 5. Rhombic
- 8. Double terminated tetragonal elongated prismatic
- 10. Elongated tetrahedrons
- 11. Trigonal flat prismatic
- 12. Di-pyramids
- 16. Protruded di-pyramids
- 18. Dumbbell fibro-radial spherules
- 20. Dodecahedron coatings

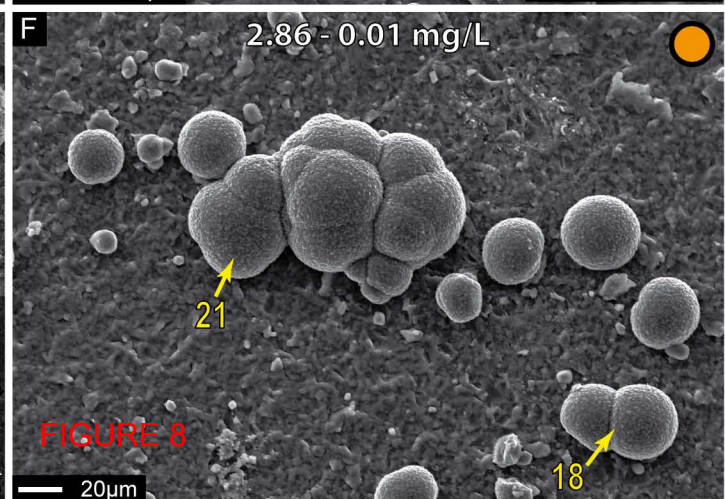
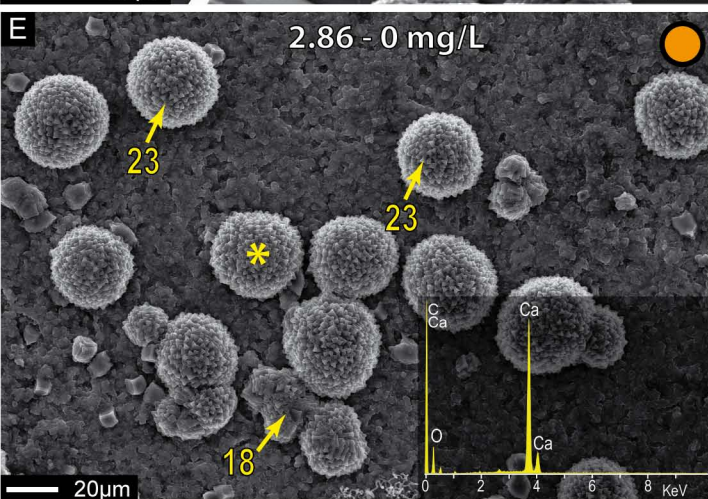
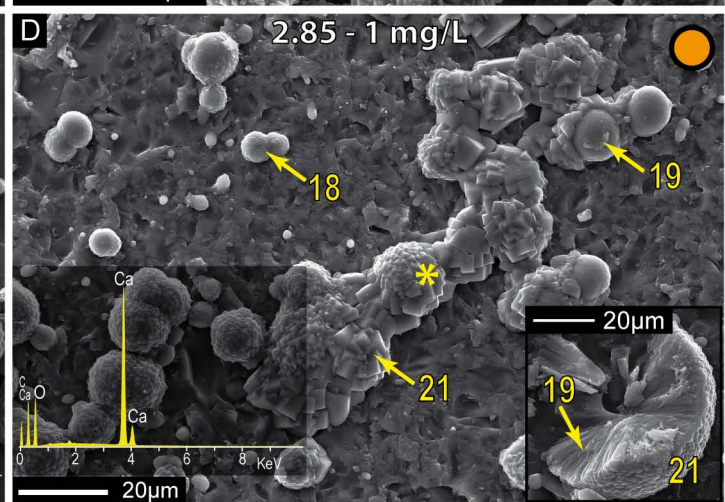
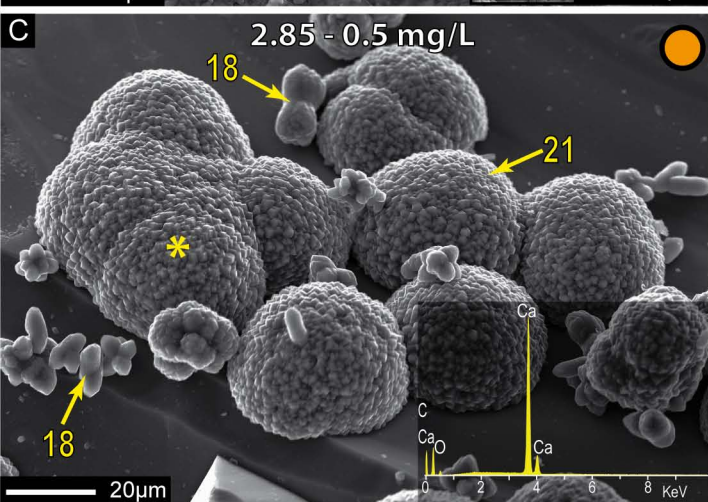
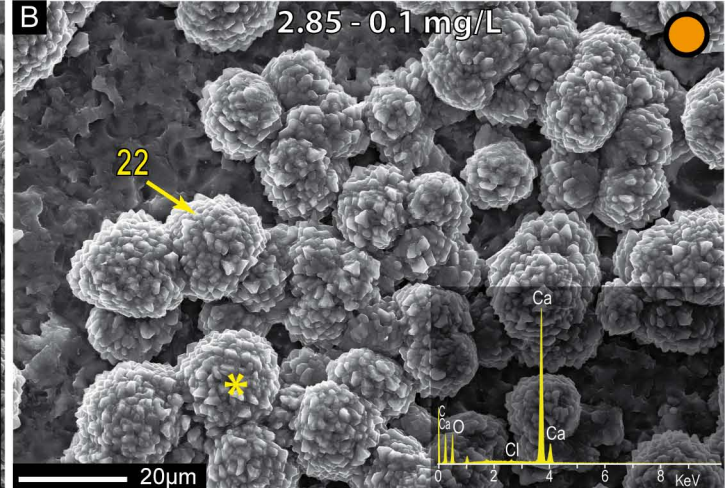
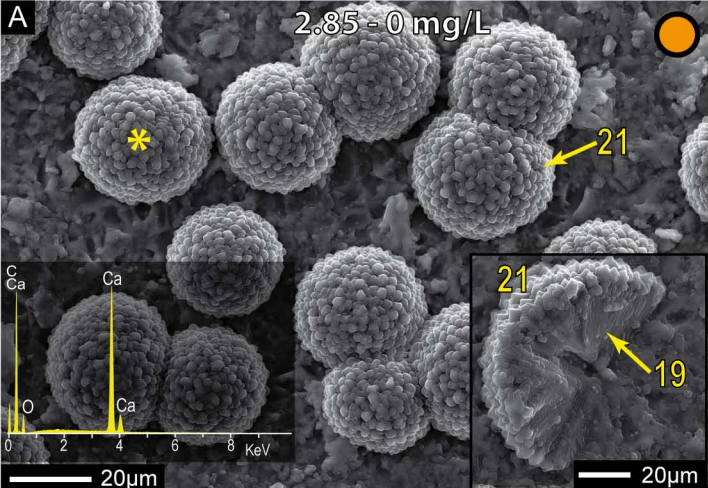
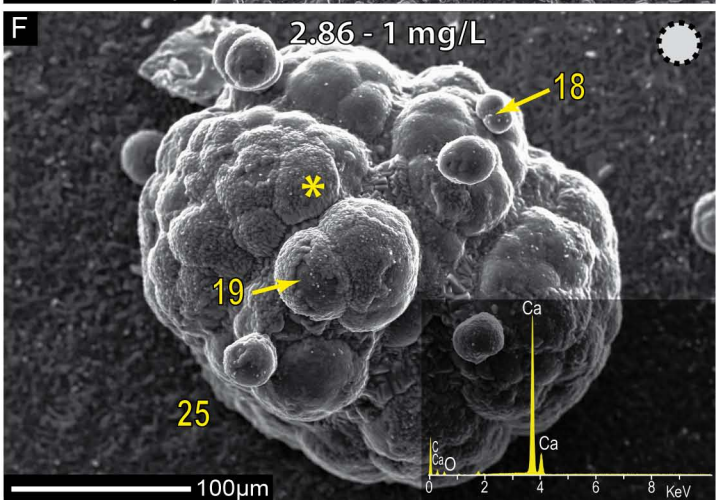
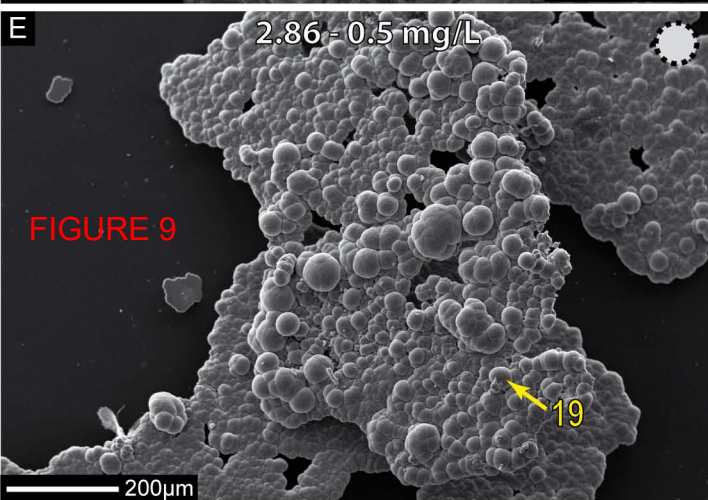
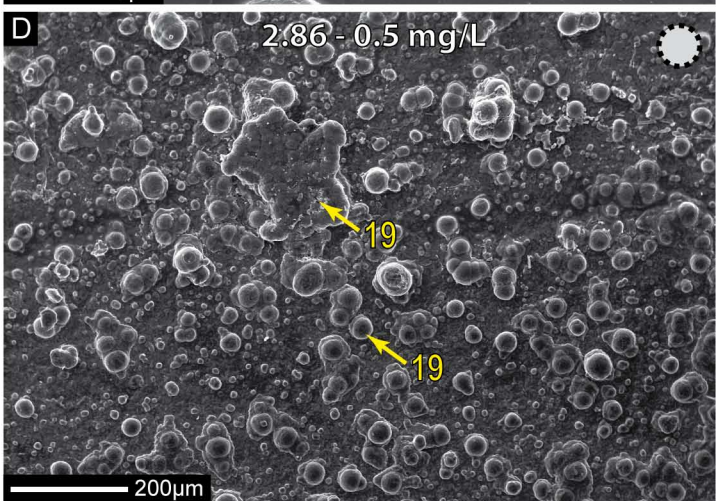
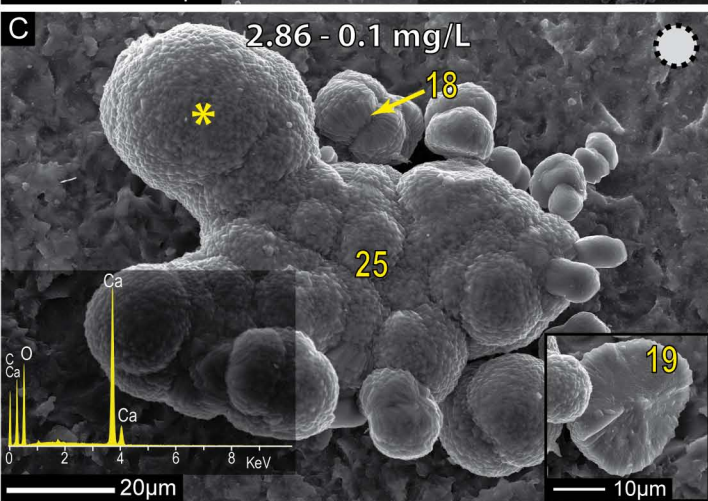
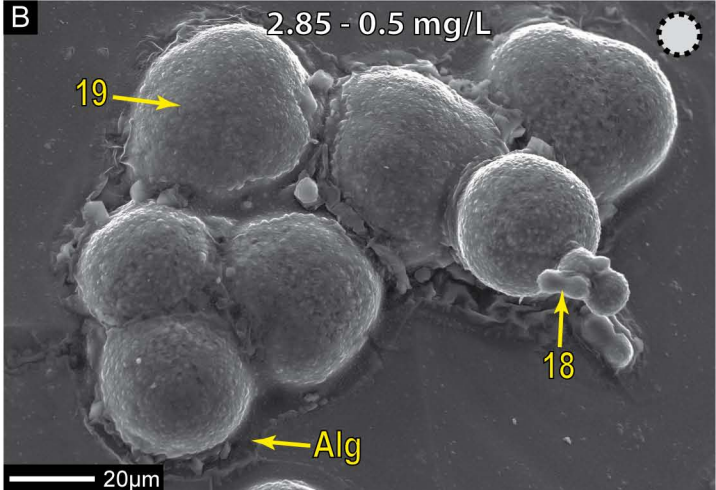
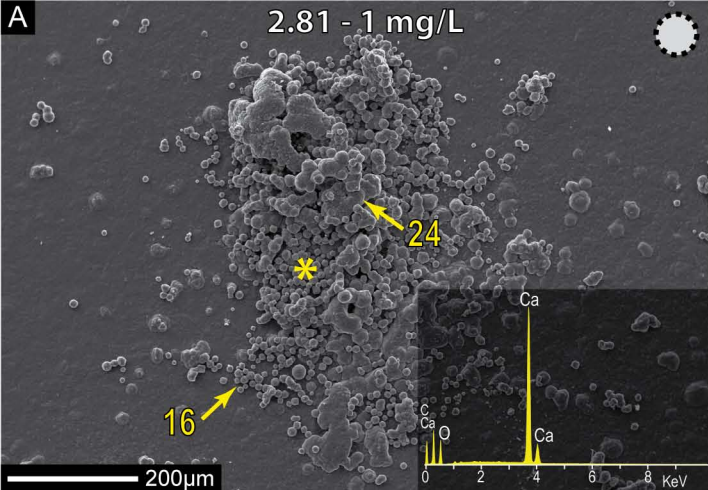


FIGURE 8

18. Dumbbell fibro-radial spherules 19. Fibro-radial spherules 21. Rhombic coatings

22. Tetrahedron coatings 23. Reinforced rhombic coatings



16. Protruded di-pyramids

18. Dumbbell fibro-radial spherules

19. Fibro-radial spherules

25. Shrub-like fibro-radial spherules

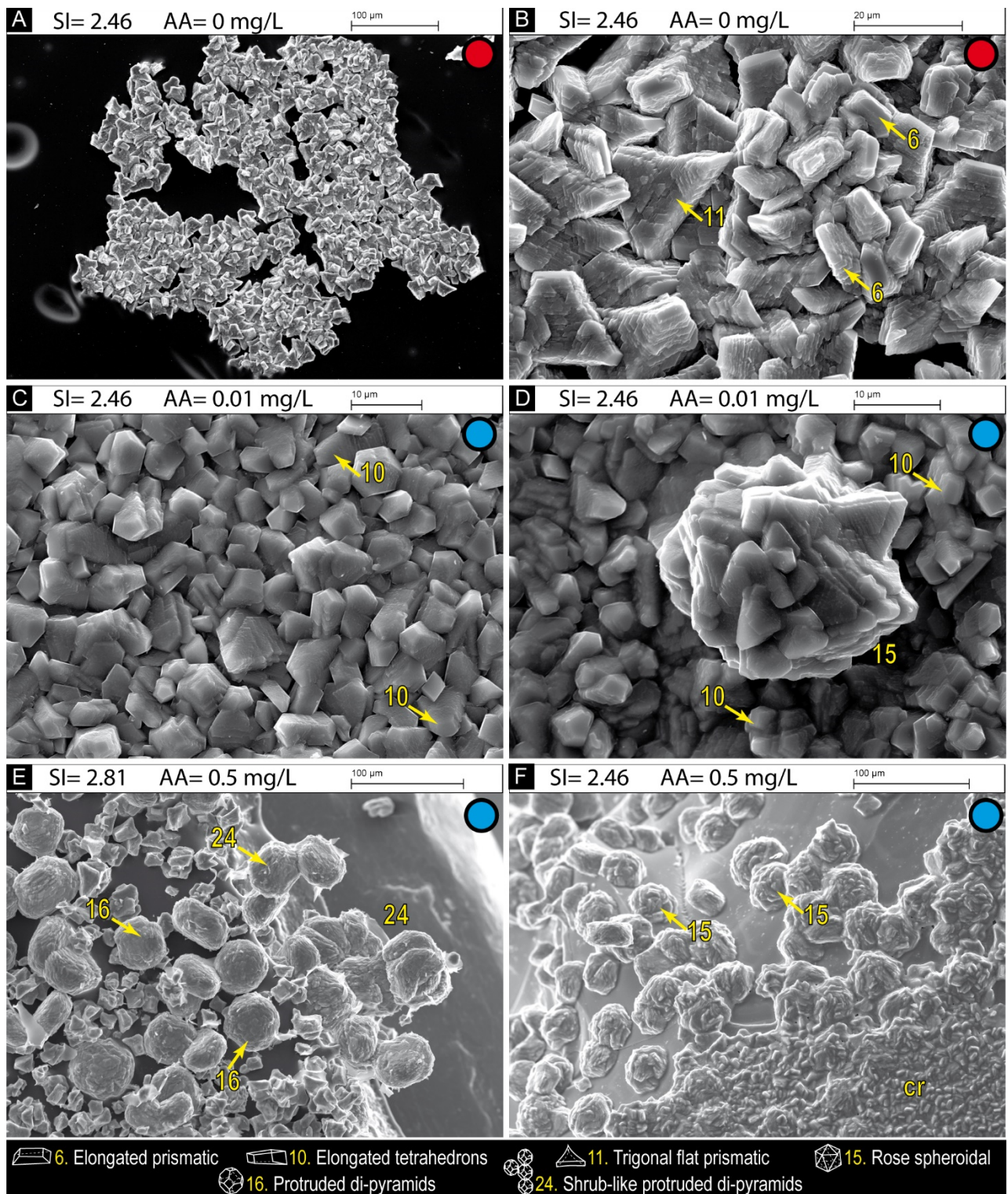


FIGURE S1. A) Floating raft clusters made up of imbricated elongated prismatic crystals and trigonal flat prismatic/faceted crystals. B) Detail of A showing trigonal flat prismatic/ faceted calcite crystals, and elongated prismatic forms. C) Tightly fitted crust of subhedral elongated tetrahedron calcite particles. D) Subhedral elongated tetrahedron calcite particles underlying bigger ‘rose-like’ calcite spheroidal particles. E) Calcite di-pyramids with protruded and rounded corners can form vertically stacked patchy clusters with positive. These are growing on the edge of the slide. F) ‘Rose-like’ spheroidal particles with rhombic imbricated crystals coalescing forming clusters, or dense crusts (cr). Saturation index and alginic contents are annotated on top, and coloured circle refers to domains in Fig. 4A and B. Numbers refer to crystal terminology attached to the bottom side.

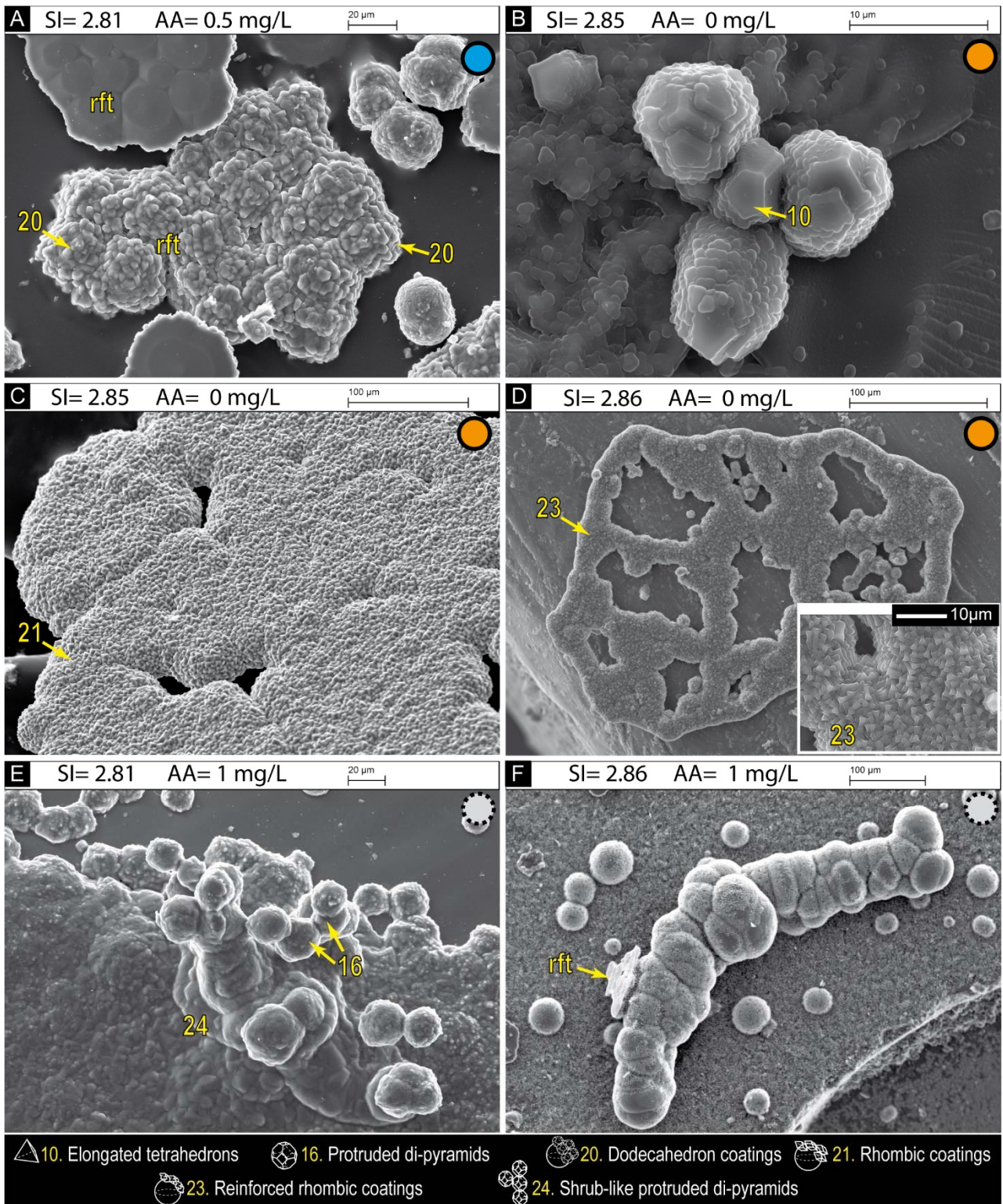
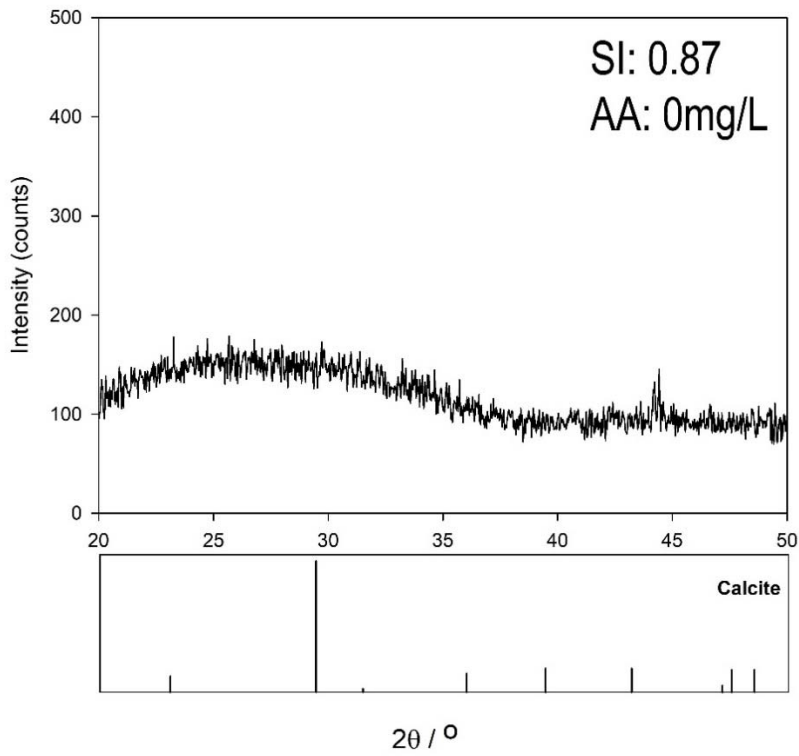
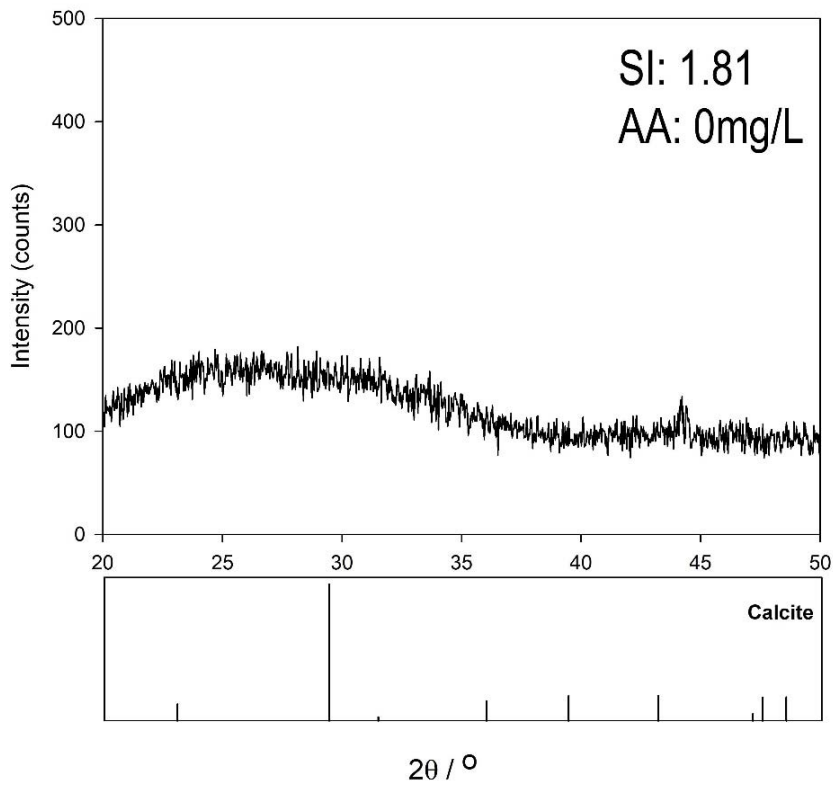
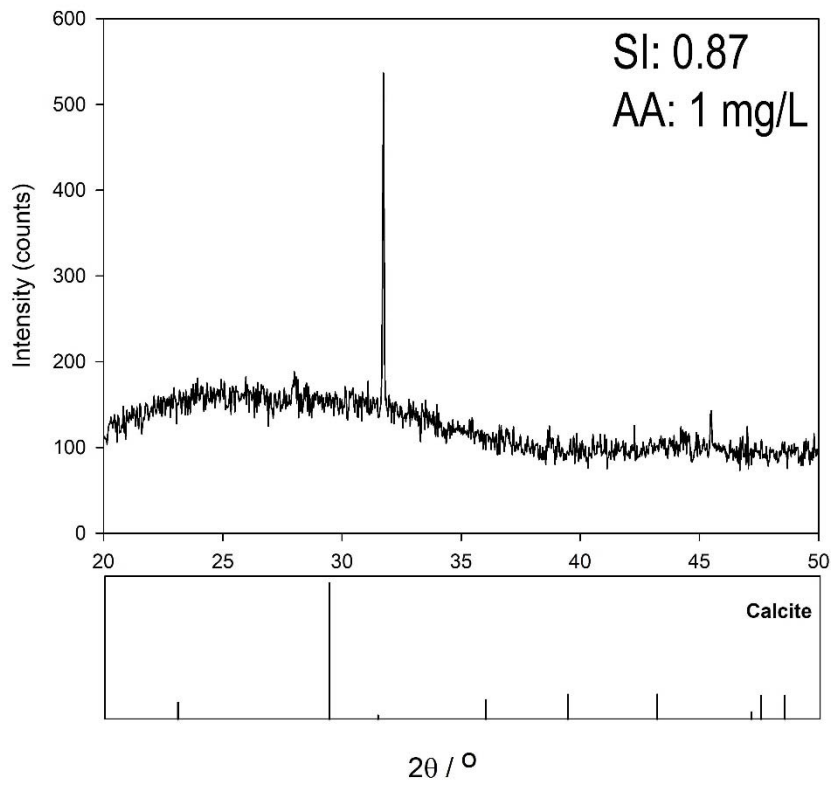
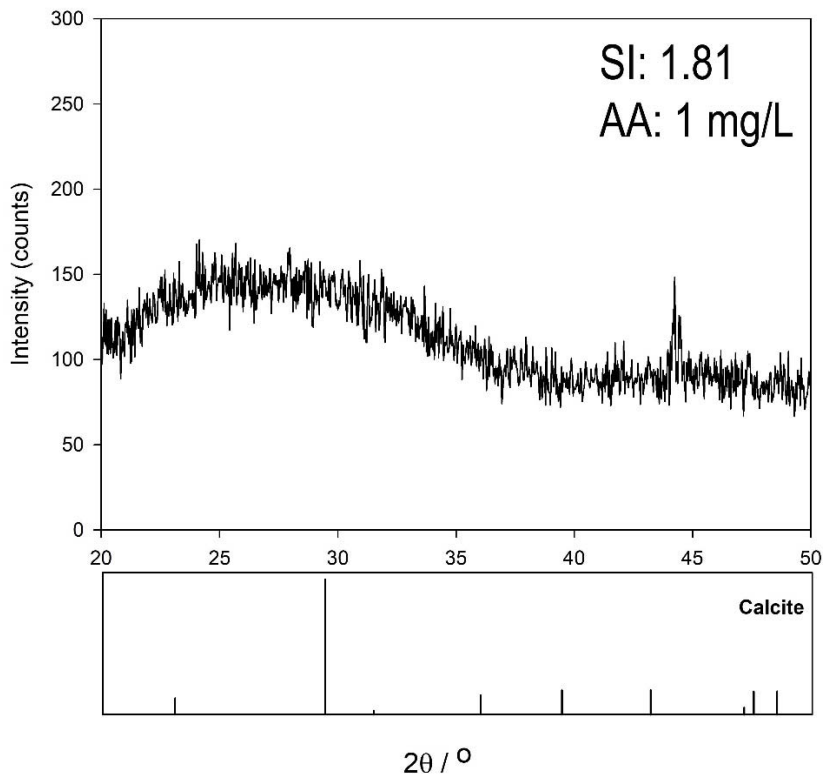
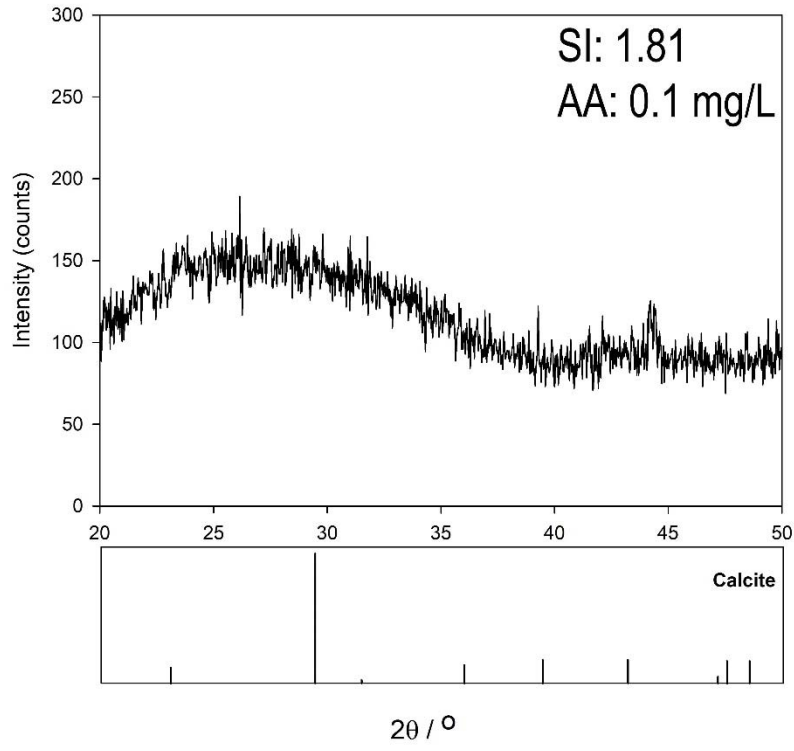


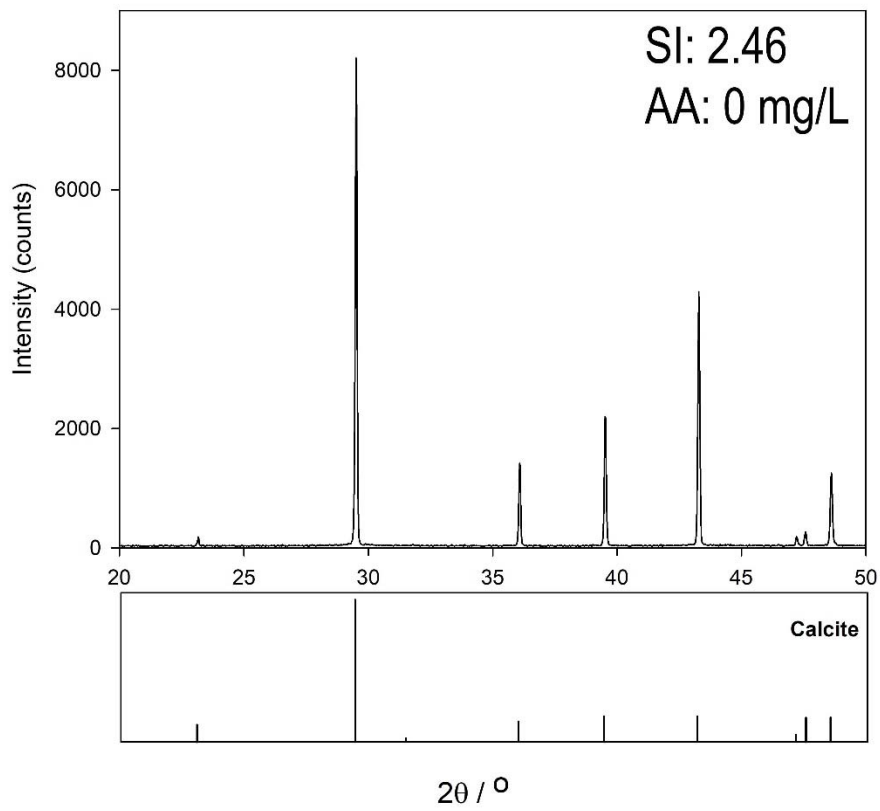
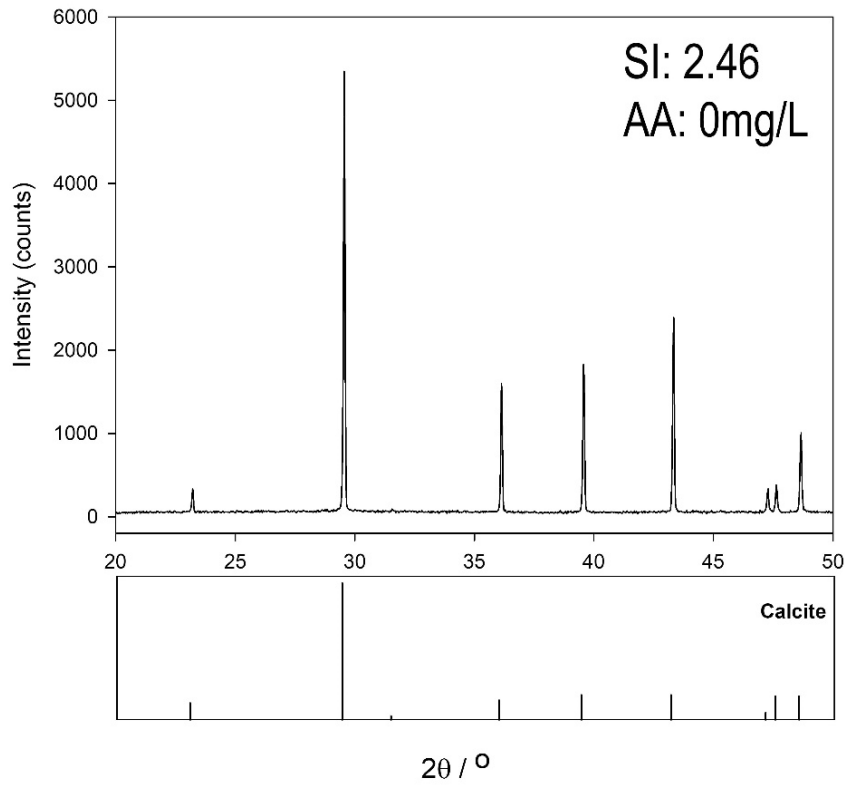
FIGURE S2. A) The downward part of floating raft (rft) are made up of tightly-fitted crusts of spherulitic calcite bodies coated by dodecahedron calcite crystals. B) Individual tiny and elongated tetrahedron prismatic seeding some spherular aggregates. C) Floating rafts made up of densely fitted fibro-radial spheroidal calcite particles coated by rhombic euهدral calcite crystals. D) Floating rafts made up fibro-radial spheroidal calcite particles coated by reinforced rhombic crystals (inset). E) Vertically growing spheroidal calcite grains composed of protruded di-pyramid calcite components. F) Elongated globular bunches expanding laterally are made up of tightly fitted spheroidal calcite particles. Saturation index and alginic contents are annotated on top, and coloured circle refers to domains in Fig. 4A and B. Numbers refer to crystal terminology attached to the bottom side.

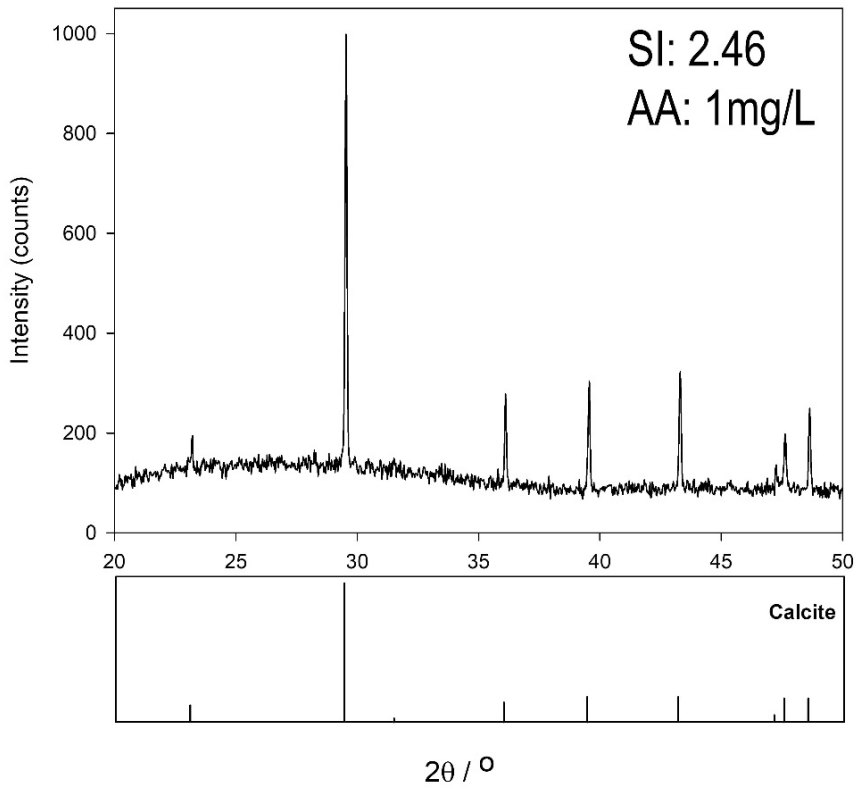
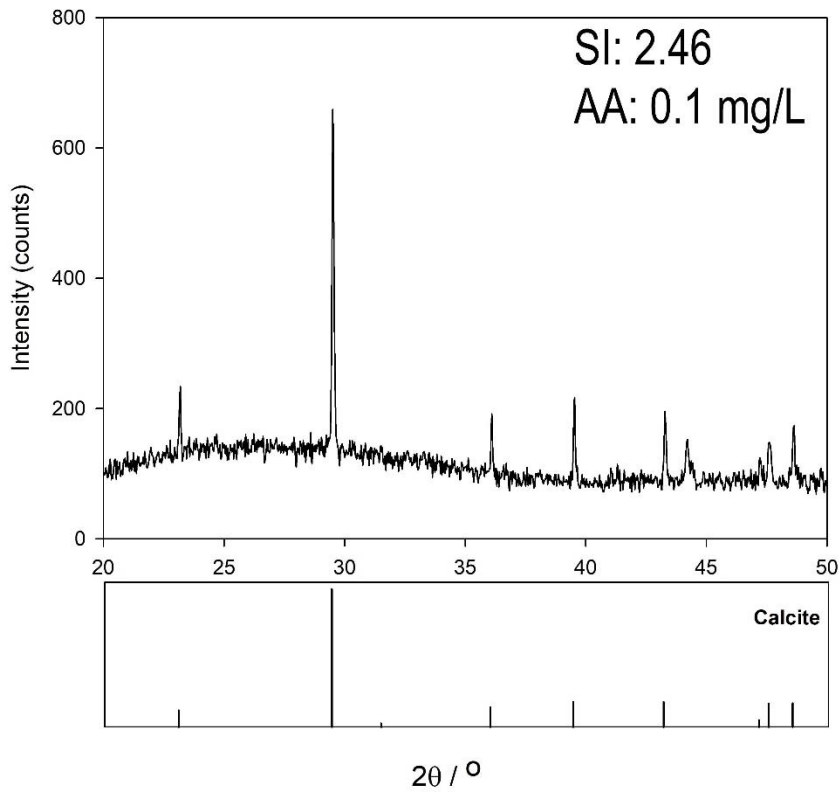
FIGURE S3. X-ray powder diffraction patterns (XRD) measured between 20 and 50 degrees (2θ range) on solids taken in the solids precipitated from experiments. The lower set of lines indicates the expected peak positions and approximate intensities for a pure sample of calcite. SI: saturation index, AA: alginic acid concentration.

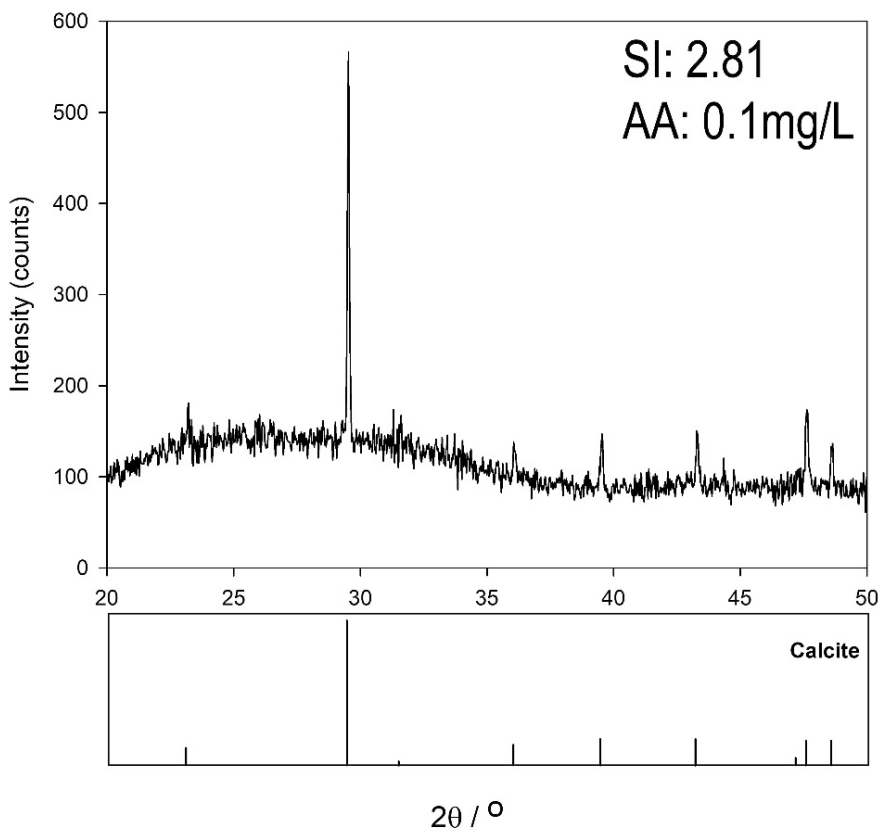
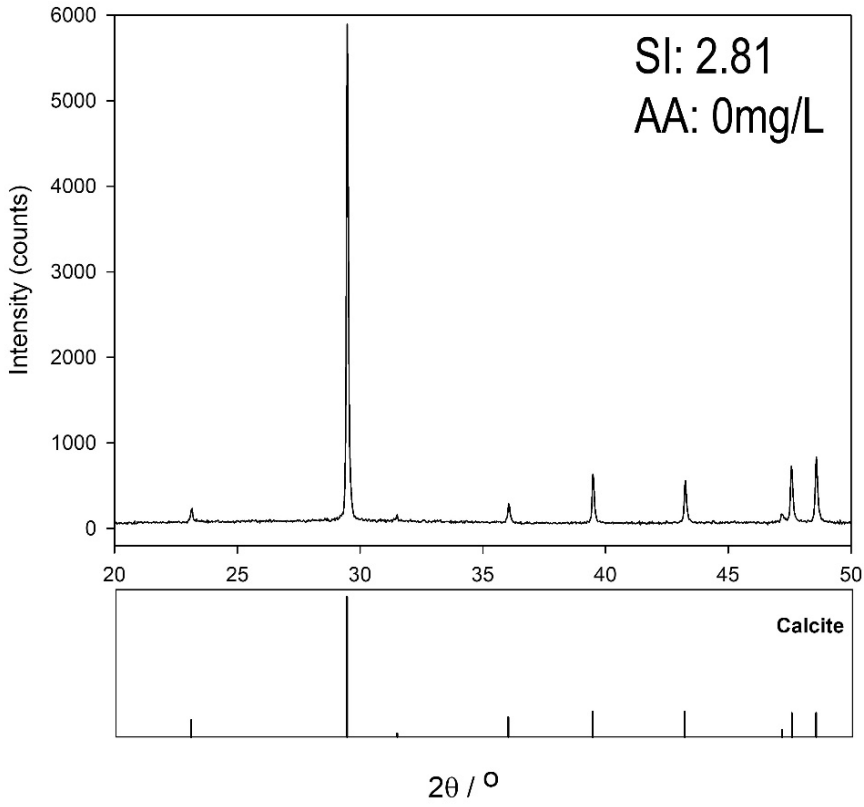


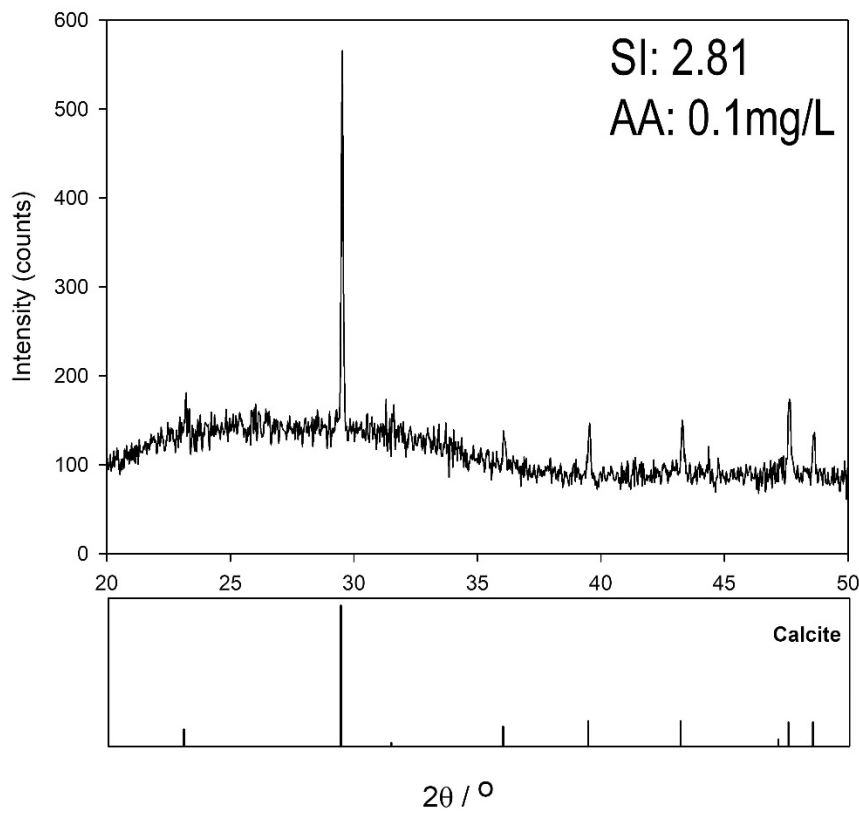
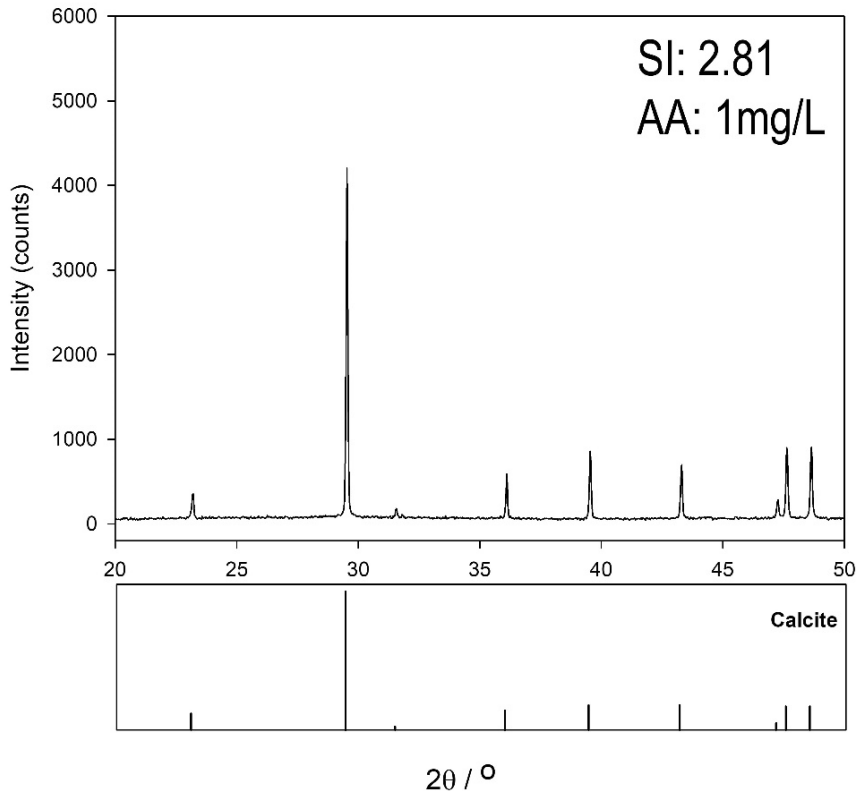


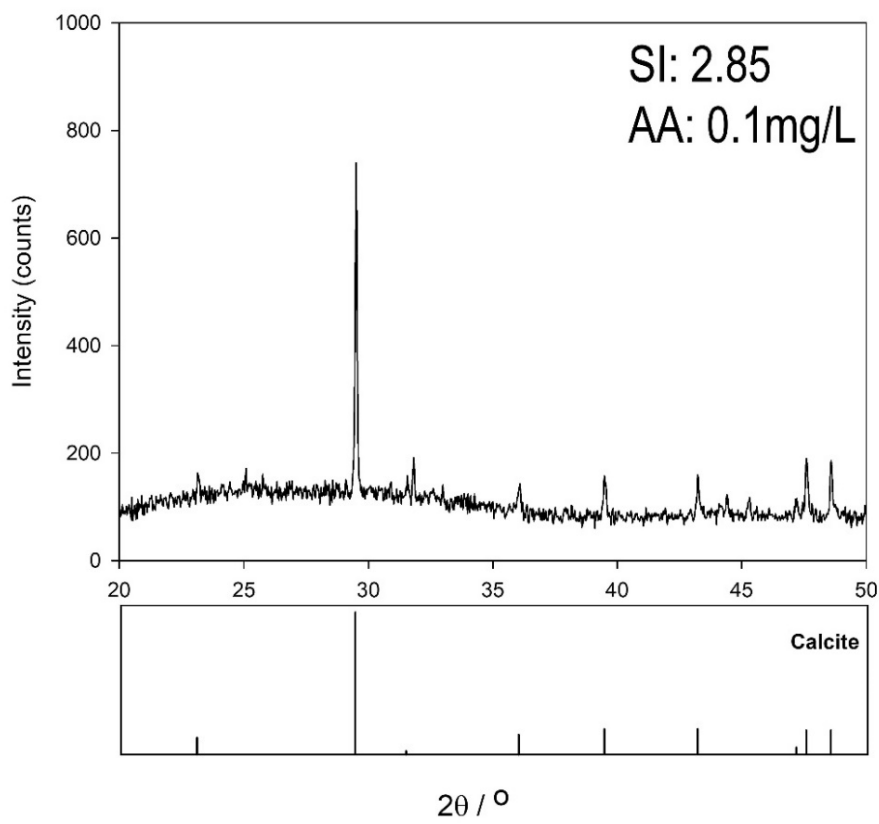
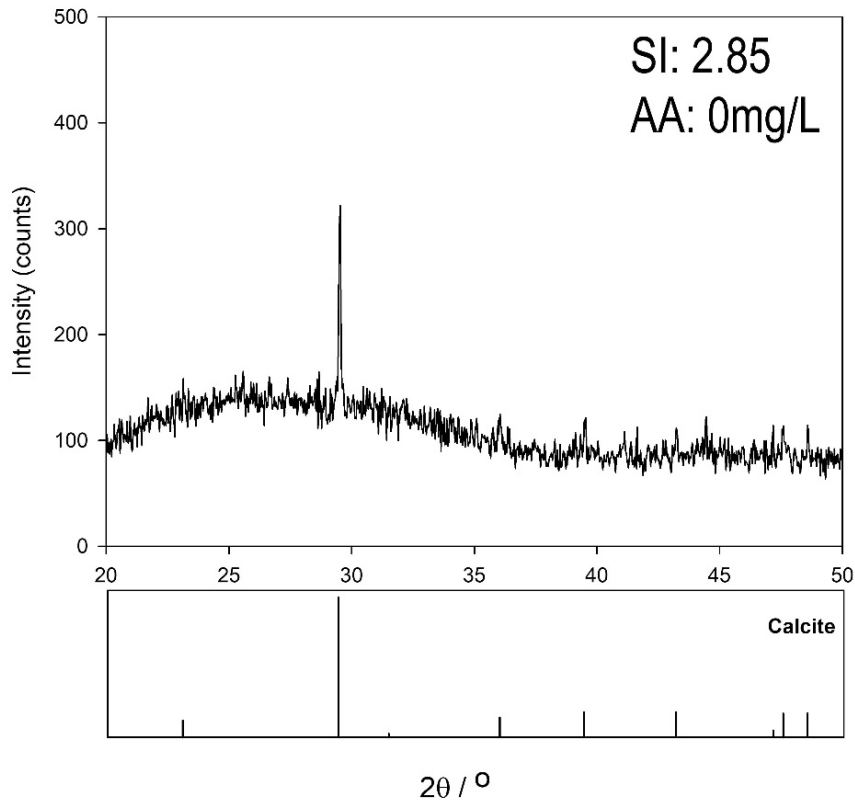


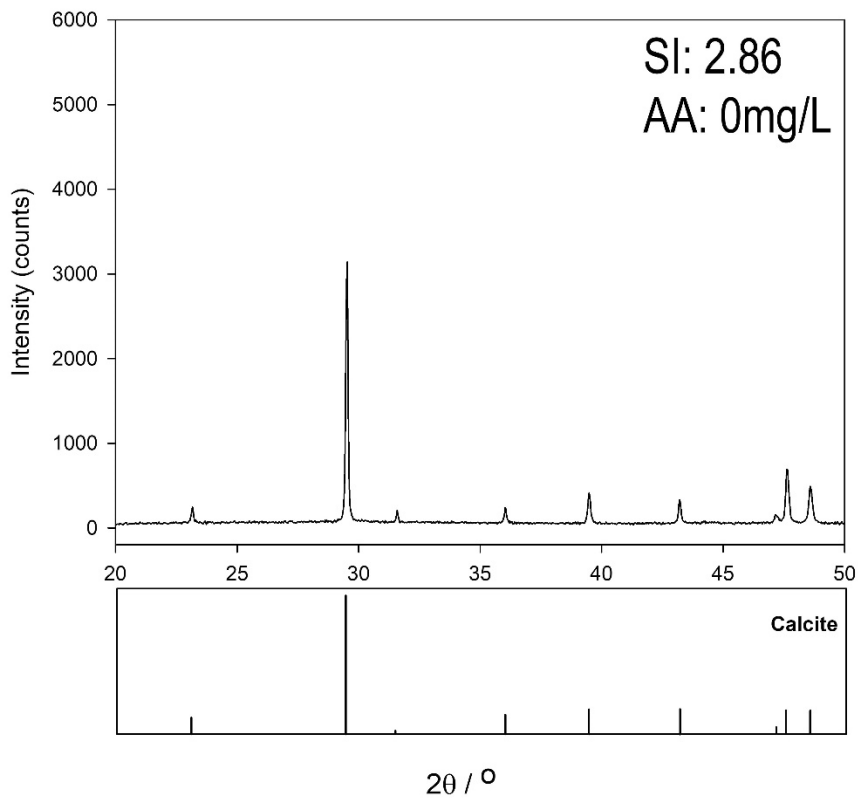
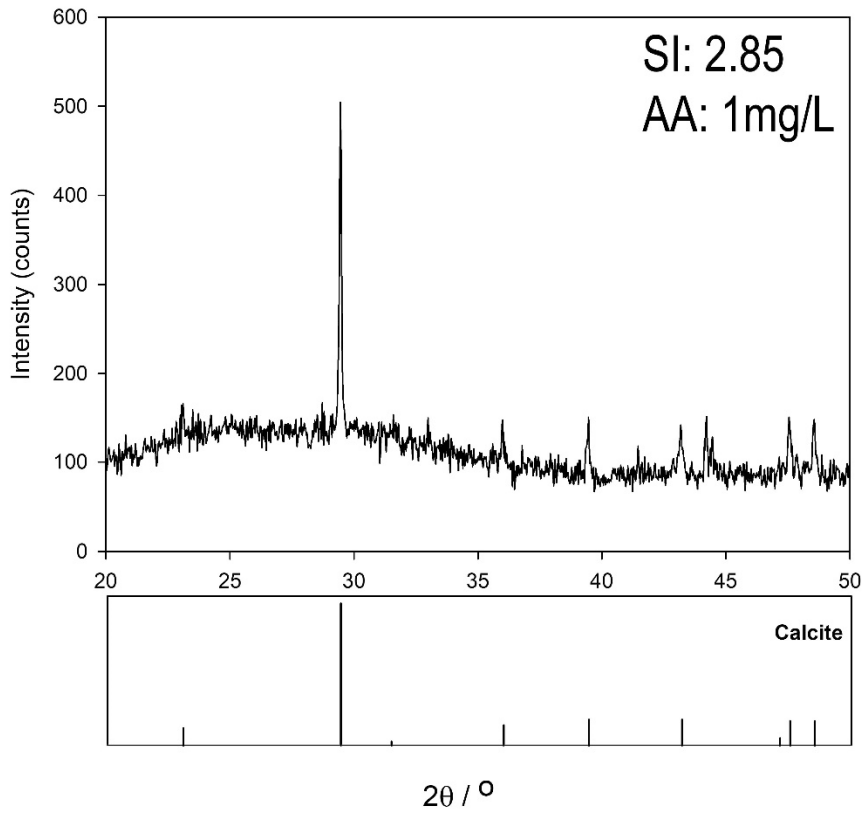


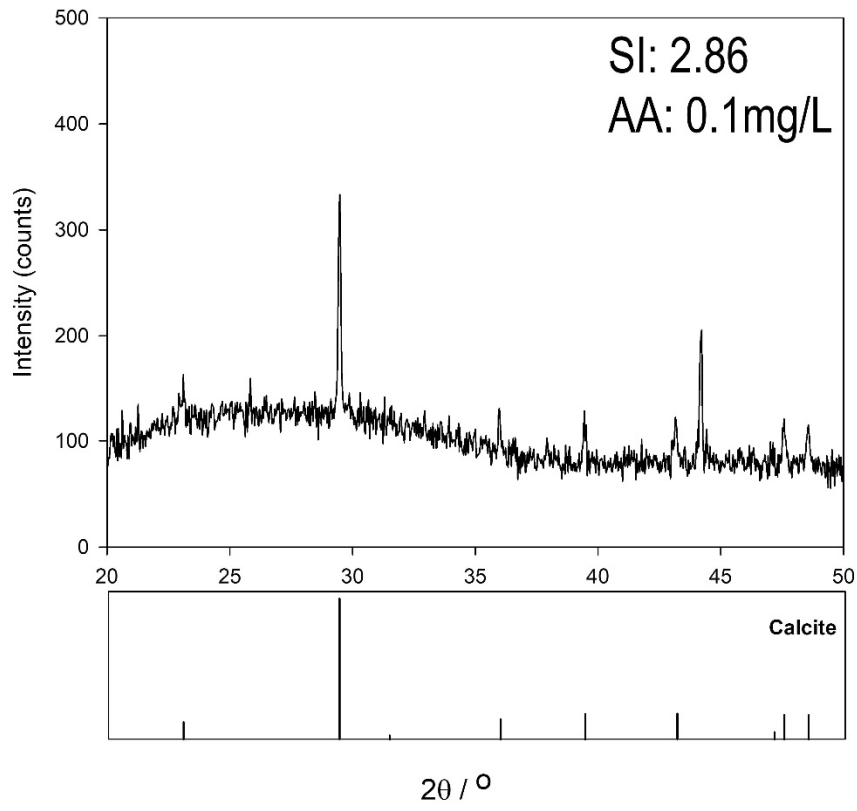












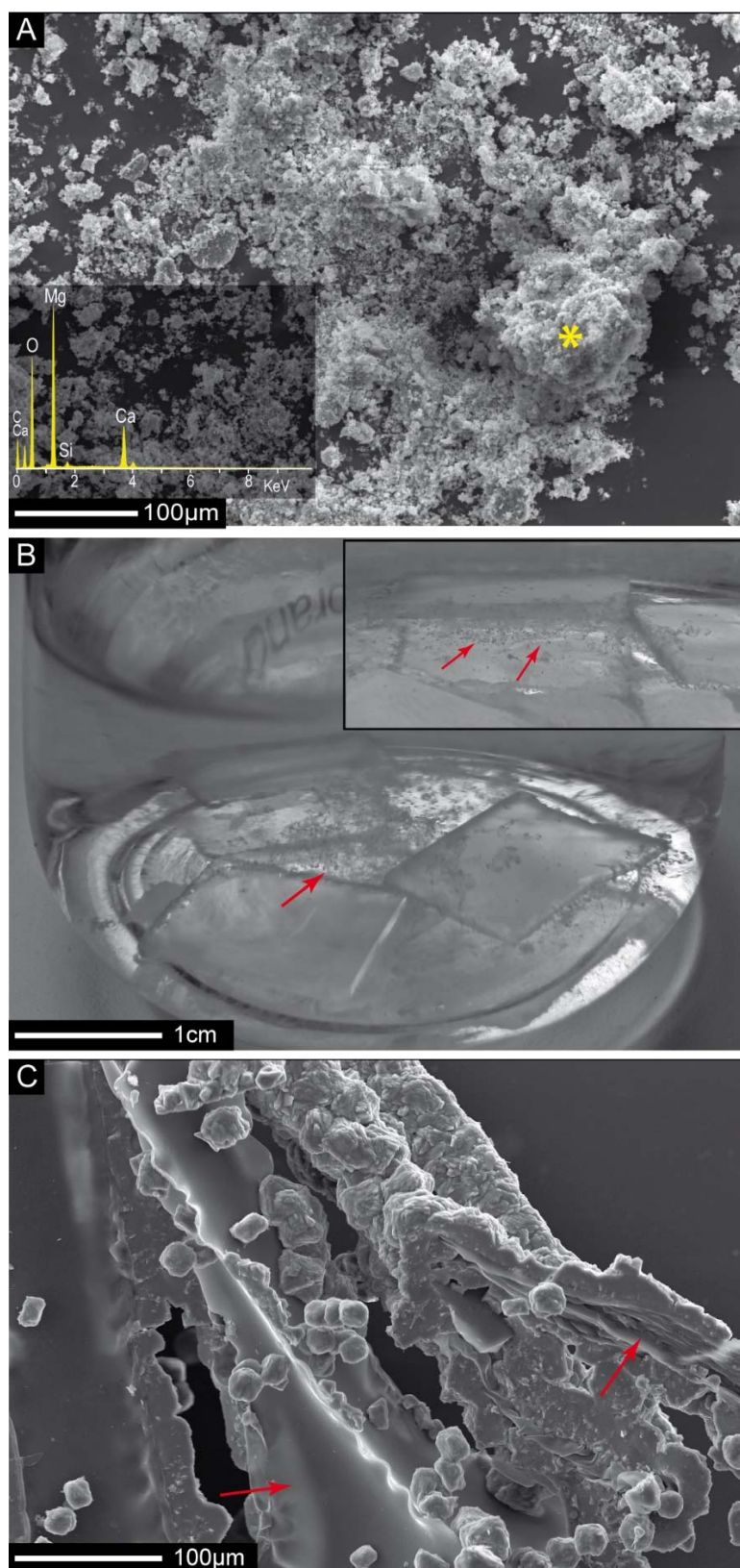


FIGURE S4. A) SEM image showing the Mg-rich carbonate powder left in the parental solution prepared at pH10. EDS spot analysis on the residue. B) Alginic acid hydrogels formed in the bottom of the flasks (arrows) under SI = 2.46 and 1 mg/L of alginic acid. Inset: detail showing tiny calcite crystals growing in the gels. C) Di-pyramid calcite crystals distributed around dried organic gels (arrows) formed under SI = 2.46 and 0.1 mg/L of alginic acid.